

Security Optimization of Exposure Region-Based Beamforming With a Uniform Circular Array

Yuanrui Zhang, Roger Woods^{ib}, Senior Member, IEEE, Youngwook Ko,
Alan Marshall, Senior Member, IEEE, and Junqing Zhang^{ib}

Abstract—This paper investigates the impact of a uniform circular array (UCA) in the context of wireless security via exposure region-based beamforming. An improvement is demonstrated for the security metric proposed in our previous paper, namely, the spatial secrecy outage probability (SSOP), by optimizing the configuration of the UCA. Our previous paper focused on formalizing the SSOP concept and exploring its applicability using a uniform linear array example. This paper proposes the UCA as a superior candidate because it is more robust against the effects of mutual coupling. The UCA's SSOP configuration is explored and a special expression is derived from the general expression for the first time, and a closed-form upper bound is then generated to facilitate analysis. By carefully designing the UCA structure particularly the radius, an SSOP optimization algorithm is derived and explored for mutual coupling. It is shown that the information leakage to eavesdroppers is reduced while the legitimate user's received signal quality is enhanced due to the use of beamforming.

Index Terms—Physical layer security, beamforming, exposure region, spatial secrecy outage probability, uniform circular array.

I. INTRODUCTION

WIRELESS communication is vulnerable to passive eavesdropping due to its broadcast nature. Physical layer security exploits the unique and unpredictable features of wireless channels such as fading and has shown a great potential to secure future wireless technologies [1], [2]. This technique dates back to Wyner's seminal work on the wiretap channel model [3], which has triggered much fruitful research and has been extended to various channel models, such as fading channels and multiple antenna channels [4]–[7].

In the physical layer security scenario with legitimate users wishing to carry out secure communication with eavesdroppers

observing the transmissions, the channel of the legitimate user in Wyner's wiretap channel model is required to be better than that of the eavesdroppers, at least for a fraction of realizations in the case of fading channels [4]. When the legitimate transmitter is equipped with multiple antennas or an antenna array, beamforming is an effective technique to enlarge the difference of the legitimate users' and eavesdroppers' channel quality and can be achieved by exploiting the channel state information (CSI) [8] or the location information [9].

Beamforming can be used to create physical regions within which any user can correctly receive the message [10]–[13]; the area was defined as an 'exposure region' (ER) in [10]. However, these regions were not based on information-theoretic parameters, such as secrecy capacity or secrecy outage probability (SOP) [4], and thus lacked a quantitative measure of the security level. On the other hand, some information theoretical based methods lacked of the analysis from a physical perspective, for example, the aspect of antenna arrays [14]–[18].

In our previous work [19], we proposed an ER-based beamforming approach which led to the derivation of the spatial secrecy outage probability (SSOP) from an information-theoretic perspective and links with the antenna array configuration. Fig. 1 illustrates a transmitter (Alice) with an antenna array that communicates to a legitimate user (Bob) in the presence of eavesdroppers (Eves) with their location distribution following a Poisson point process (PPP); this hints towards the utilization of location in the Wyner's channel model. The ER is defined by the physical region where any PPP distributed Eve causes secrecy outage to the legitimate transmission in the Rician fading channel. In [19], the secrecy outage caused by PPP distributed Eves is quantitatively measured by the SSOP that is derived from the ER. The general expression of the SSOP for any type of array is derived and the uniform linear array (ULA) is used as an example to explore the properties of the array parameters.

Based on the knowledge of the previous work, we advance knowledge in this paper by optimizing the array parameters. The uniform circular array (UCA) is chosen rather than the ULA because of practical considerations, namely mutual coupling. Mutual coupling is the electromagnetic interaction between the antenna elements of an array and is always associated with multiple antenna techniques [20], [21]. In [22], it has been shown that linear arrays are susceptible to mutual coupling, thus rendering no effective optimum solution for

Manuscript received March 27, 2017; revised August 5, 2017 and September 27, 2017; accepted October 24, 2017. This work was supported by the US-Ireland R&D Partnership USI033 WiPhyLoc8 grant involving Rice University (USA), University College Dublin (Ireland) and Queen's University Belfast (Northern Ireland). The associate editor coordinating the review of this paper and approving it for publication was J. Yuan. (*Corresponding author: Roger Woods.*)

Y. Zhang, R. Woods, Y. Ko, and J. Zhang are with the School of Electronics, Electrical Engineering and Computer Science, Queen's University Belfast, Belfast BT9 5AH, U.K. (e-mail: yzhang31@qub.ac.uk; r.woods@qub.ac.uk; y.ko@qub.ac.uk; jzhang20@qub.ac.uk).

A. Marshall is with the Department of Electrical Engineering and Electronics, University of Liverpool, Liverpool L69 3GJ, U.K. (e-mail: alan.marshall@liverpool.ac.uk).

Color versions of one or more of the figures in this paper are available online at <http://ieeexplore.ieee.org>.

Digital Object Identifier 10.1109/TCOMM.2017.2768516

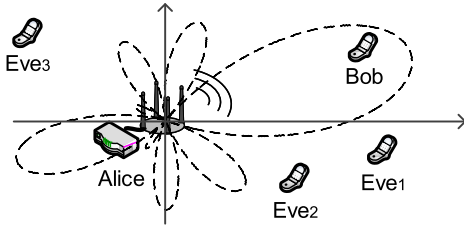


Fig. 1. The enclosed area surrounding Bob illustrates the ER created using a circular antenna array.

minimizing the SSOP. On the other hand, the UCA is less affected and produces a more symmetric beam pattern around 360° [23]. Thus, it is chosen as the candidate to exhibit the optimization of the array parameters, especially the radius.

We assume that Bob's location information is available at Alice, which is similar to that used in [9]. For example, Bob could send his own location information to Alice, if he wishes to be served by Alice with additional security features. Alice exploits Bob's location information to perform the beamforming.

In fading channels, the security performance of the aforementioned system, i.e., Alice using beamforming to enlarge the difference between Bob's and Eves' channels, can be expressed in terms of secrecy outage. In [24], the secrecy outage probability (SOP) for a single Eve is given by the probability that Eve's channel capacity is higher than a certain threshold; this is defined by the difference between the rate of the transmitted codewords and that of the confidential information, conditioned on Bob's channel capacity being larger than the rate of the transmitted codewords. In other words, the ER is an enclosed area within the boundary where Eve's channel capacity is just equal to that threshold. As Eve's channel capacity is random due to fading, the boundary of the ER shifts. In Fig. 1, the dashed curve depicts an ER boundary for a deterministic channel, which resembles the shape of the array pattern.

Intuitively, the smaller the ER is, the less possible that Eves are located inside the ER, and therefore the more secure the transmission will be. The overall secrecy outage caused by PPP distributed Eves, i.e., SSOP, is calculated with the aid of stochastic geometry theory, which links the security performance with the UCA parameters. This paper builds substantially on our previous work [19], [25] by investigating the SSOP with respect to UCA parameters in Rician fading channel and creating an optimization algorithm which minimizes the SSOP by adjusting the radius. In addition, the impact of mutual coupling is examined on the SSOP using a numerical simulation tool, i.e., NEC [26]. In essence, this sets the scene for setting secure regions in wireless networks. The main contributions of this paper are:

- Deriving the expression of the SSOP for the UCA and the closed-form expression of its upper bound for the first time, thus revealing the relationship between the security performance and various parameters, especially the radius of the UCA.
- Based on the expressions of the SSOP for the UCA, the first investigation of the security performance of

ER-based beamforming for a Rician fading channel with respect to radius is presented. Simulation and numerical results are covered, which show how the behavior of averaged SSOP varies with the radius.

- An optimization algorithm is derived based on the above analysis, which enhances the security level by optimizing the radius for all of Bob's possible angles. The impact of the mutual coupling with the radius is compared with the optimization algorithm and shows that while the algorithm in general is valid, the optimum value needs to be calculated using numerical data.

The rest of the paper is organized as follows. In Section II, the system model is introduced and the definitions of the ER and the SSOP are presented. In Section III, the closed-form expression of the upper bound is derived and from this the impact of the radius of the UCA is analyzed. In Section IV, the optimization problem is established and analyzed with respect to the UCA array parameters; an algorithm is then created with the aim of decreasing the SSOP. In Section V, simulation and numerical results are given. Section VI concludes the paper.

II. EXPOSURE REGION AND SPATIAL SECRECY OUTAGE PROBABILITY

A. System Model

As the paper builds on [19], the system model is the same except for the UCA aspect. For this reason, the essential symbols, concepts and derivations for the UCA are described briefly to avoid repetition. Let's assume that Alice is equipped with an antenna array while Bob and Eves have a single antenna. As shown in Fig. 1, Alice is located at the origin point. For convenience, assume that the first element of the UCA is on the positive x-axis. The coordinate is denoted by $z = (d, \theta)$, and subscripts B and E_i are used to represent Bob and the i^{th} Eve respectively, $\forall i \in \mathbb{N}^+$. A general user's location is referred to by z when no subscript is specified. Eves are assumed to be non-colluding and distributed by a homogeneous PPP, Φ_e with density λ_e [27].

On the transmitter side, the UCA has N elements and radius R , and the array vector of UCA is $\mathbf{s}(\theta) = [e^{-j\phi_1(\theta)}, \dots, e^{-j\phi_i(\theta)}, \dots, e^{-j\phi_N(\theta)}]^T$, $\theta \in [0, 2\pi]$, where $\phi_i(\theta) = kR \cos(\theta - \psi_i)$, and $\psi_i = 2\pi(i-1)/N$ is the angular location of the i^{th} element [28] and $k = 2\pi/\lambda$, where λ is the wavelength of the carrier signal. P_t is the transmit power. Given Bob's location information, θ_B , the beamforming weight vector can be set as $\mathbf{w} = \mathbf{s}(\theta_B)/\sqrt{N}$.

Assume a Rician channel with factor K . The channel gain vector is given by

$$\mathbf{h}(z) = d^{-\beta/2} \left(\sqrt{\frac{K}{K+1}} \mathbf{s}(\theta) + \sqrt{\frac{1}{K+1}} \mathbf{g} \right), \quad (1)$$

where $d^{-\beta/2}$ denotes the large-scale path loss with the path loss exponent β of typical values between 2 and 6. The line-of-sight (LOS) component is $\sqrt{\frac{K}{K+1}} \mathbf{s}(\theta)$; the non-LOS component is $\sqrt{\frac{1}{K+1}} \mathbf{g}$, where $\mathbf{g} = [g_1, \dots, g_i, \dots, g_N]^T$, $g_i \sim \mathcal{CN}(0, 1)$, and the elements of \mathbf{g} are independent. Thus, the received signal at z is the sum of the beamforming

178 weighted signals and noise, which can be expressed by $r(z) =$
 179 $\sqrt{P_t} \mathbf{h}^T(z) \mathbf{w}^* x + n_W$, where x is the modulated symbol with
 180 unit power and n_W is the additive white Gaussian noise with
 181 zero mean and variance σ_n^2 .

182 For the ease of subsequent mathematical derivations, let \tilde{h}
 183 be an equivalent channel factor, i.e.,

$$184 \quad \tilde{h} = \mathbf{h}^T(z) \mathbf{w}^* = \sqrt{\frac{K}{K+1}} G(\theta, \theta_B) + \sqrt{\frac{1}{K+1}} g, \quad (2)$$

185 where $G(\theta, \theta_B) = \mathbf{s}(\theta) \mathbf{s}^*(\theta_B) / \sqrt{N}$ is an array factor for any
 186 array type and $g \sim \mathcal{CN}(0, 1)$. According to (2), $|\tilde{h}|^2$ can be
 187 decomposed as follows:

$$188 \quad |\tilde{h}|^2 = \frac{K G^2(\theta, \theta_B)}{K+1} + \frac{g_{Re}^2 + g_{Im}^2}{K+1} + \frac{2\sqrt{K} G(\theta, \theta_B)}{K+1} g_{Re}, \quad (3)$$

189 where g_{Re} and g_{Im} are the real and imaginary part of g ,
 190 so, $g_{Re}, g_{Im} \sim \mathcal{N}(0, \frac{1}{2})$. For the UCA, the array factor was
 191 derived in [28] and is given by

$$192 \quad G(\theta, \theta_B) = \frac{1}{\sqrt{N}} \sum_{i=1}^N e^{jkR[\cos(\theta_B - \psi_i) - \cos(\theta - \psi_i)]}. \quad (4)$$

193 The channel capacity, denoted by $C(z)$, is given by

$$194 \quad C(z) = \log_2 \left(1 + \frac{P_t |\tilde{h}|^2}{\sigma_n^2 d^\beta} \right). \quad (5)$$

195 For convenience, let $C_B = C(z_B)$ and $C_{Ei} = C(z_{Ei})$ denote
 196 the channel capacities of Bob and the i^{th} Eve hereinafter. Due
 197 to the fact that $|\tilde{h}|^2$ scales with $G(\theta, \theta_B)$, a proper design of
 198 $G(\theta, \theta_B)$ can improve C_B while decreasing C_{Ei} .

199 B. Definitions for ER and SSOP for UCA

200 As in [24], let R_B and R_s be the rate of the transmitted code-
 201 words and the rate of the confidential information, respectively.
 202 A secrecy outage event occurs when Eve's channel capacity is
 203 higher than the difference $R_B - R_s$ conditioned on $C_B \geq R_B$,
 204 and the probability of such an event is the SOP. Note that
 205 here two cases are differentiated, i.e., secrecy outage caused
 206 by any Eve conditioned on $C_B \geq R_B$ and data outage given
 207 by $C_B < R_B$. In the latter case, it is typical outage with no
 208 secrecy and thus no secrecy outage. Therefore, the data outage
 209 is not part of the secrecy outage and is beyond the scope of
 210 this paper. In practice, Bob can transmit a one bit feedback to
 211 Alice indicating whether the condition $C_B \geq R_B$ is satisfied.

212 The ER, denoted by Θ , is defined by the geometric region
 213 only where Eves cause the secrecy outage event, i.e., $C_{Ei} >$
 214 $R_B - R_s, \exists z_{Ei} \in \Theta$ conditioned on $C_B \geq R_B$. The boundary
 215 of ER can be derived from $C(z) > R_B - R_s$ and is given
 216 by $D(\theta) = (c_0 P_t |\tilde{h}|^2)^{1/\beta}$, where $c_0 = [\sigma_n^2 (2^{R_B - R_s} - 1)]^{-1}$
 217 is deterministic and is assumed to be constant in this paper.
 218 Thus, $D(\theta)$ is random as $|\tilde{h}|^2$ varies. When the channel is
 219 deterministic, $D(\theta)$ is also deterministic, as shown by the
 220 dashed curve in Fig. 1.

221 Let A denote the size of Θ . For PPP-distributed Eves, the
 222 probability of m Eves being inside $D(\theta)$ can be given by [27]

$$223 \quad \text{Prob}\{m \text{ Eves in } \Theta\} = \frac{(\lambda_e A)^m}{m!} e^{-\lambda_e A}. \quad (6)$$

224 Thus, the SSOP, denoted by p , can be defined by the proba-
 225 bility that any Eve is located inside $D(\theta)$.

$$226 \quad p = 1 - \text{Prob}\{0 \text{ Eve in } \Theta\} = 1 - e^{-\lambda_e A}. \quad (7)$$

227 Note that p is computed by the complementary of the proba-
 228 bility that no Eve is inside Θ . In polar coordinates, (7) can
 229 be derived by

$$230 \quad p = 1 - \exp\left[-\frac{\lambda_e}{2} c_0^{\frac{2}{\beta}} P_t^{\frac{2}{\beta}} \int_0^{2\pi} (|\tilde{h}|^2)^{\frac{2}{\beta}} d\theta\right]. \quad (8)$$

231 The smaller p is, the more secure the transmission to Bob is.
 232 Due to the fact that \tilde{h} is random channel fading, it is more
 233 interesting to study the expectation of p in (8), which reflects
 234 the averaged SSOP \bar{p} ,

$$235 \quad \bar{p} = \mathbb{E}_{|\tilde{h}|} [p]. \quad (9)$$

236 The term \bar{p} in (9) can be expressed by

$$237 \quad \bar{p} = 1 - \int_{-\infty}^{\infty} \int_{-\infty}^{\infty} \exp\left\{-\frac{\lambda_e}{2} c_0^{\frac{2}{\beta}} P_t^{\frac{2}{\beta}} \int_0^{2\pi} \left[\frac{K G^2(\theta, \theta_B)}{K+1}\right.\right. \\ 238 \quad \left.\left. + \frac{x^2 + y^2}{K+1} + \frac{2\sqrt{K} G(\theta, \theta_B)}{K+1} x\right]^{\frac{2}{\beta}} d\theta\right\} \frac{e^{-(x^2+y^2)}}{\pi} dx dy, \quad (10)$$

240 Notice that $G(\theta, \theta_B)$ is a general array factor expression. For
 241 the UCA, p and \bar{p} are obtained by substituting (4) into (8)
 242 and (10).

243 C. An Optimization Problem

244 The focus of this paper is to increase the security level of
 245 the transmission from Alice to Bob, i.e., reducing \bar{p} . To this
 246 end, \bar{p} is first analyzed against the factors in (10). Assume that
 247 the noise variance σ_n^2 , channel factors β and K , the security
 248 related parameters R_B and R_s and the density of Eves λ_e are
 249 fixed. The remaining factors are the transmit power P_t , the
 250 array factor $G(\theta, \theta_B)$ and Bob's location (d_B, θ_B) . Thus, an
 251 optimization problem can be expressed by

$$252 \quad \min \bar{p} \text{ s.t. for all } d_B, \theta_B \quad (11)$$

253 To minimize \bar{p} , the interrelationship between parameters
 254 related to Alice, i.e., P_t and $G(\theta, \theta_B)$, and Bob's location
 255 (d_B, θ_B) should be analyzed. Note that d_B does not appear
 256 in (10) and P_t has a monotonic relationship with \bar{p} . In addition,
 257 the impact of P_t and $G(\theta, \theta_B)$ on \bar{p} are independent according
 258 to (10). In this paper, when studying the impact of $G(\theta, \theta_B)$,
 259 P_t and d_B will be not be included.

260 $G(\theta, \theta_B)$ in (4) depends on the array parameters N and
 261 R as well as Bob's angle θ_B . As the number of antennas N
 262 is normally fixed for a certain UCA, the impact of R will
 263 be mainly discussed against θ_B . Due to the reflection and
 264 rotation symmetry of the UCA, the shape of $G(\theta, \theta_B)$ also has
 265 reflection and rotation symmetry regarding θ_B . An example
 266 of $G(\theta, \theta_B)$ with $\theta_B = 0, \frac{\pi}{4}$ and $N = 8$ is shown in Fig. 2.
 267 As the first element of the UCA lies on the positive x-axis, the
 268 shape of $G(\theta, \theta_B)$ for $\theta_B = \frac{\pi}{4}$ can be obtained by shifting the
 269 shape for $\theta_B = 0$ by $\frac{\pi}{4}$, and vice versa. At the same time,
 270 the two shapes are symmetric regarding to $\theta_B = \frac{\pi}{8}$. In general,

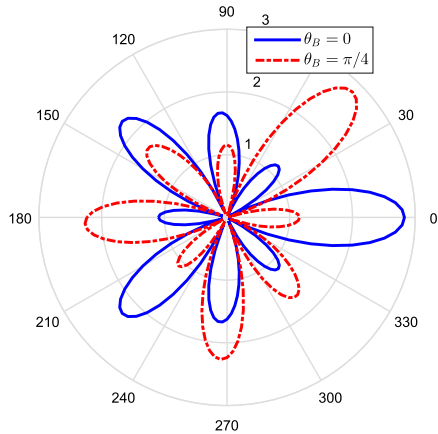


Fig. 2. $G(\theta, \theta_B)$ for $\theta_B = 0$ and $\theta_B = \frac{\pi}{4}$. $N = 8$ and $R = 0.8\lambda$.

271 $G(\theta, \theta_B)$ at $\pm(\theta_B \pm 2\pi/N)$ are of the same shape. Therefore,
 272 it suffices to study $G(\theta, \theta_B)$ only in $\theta_B \in [0, \frac{\pi}{N}]$ instead of
 273 $[0, 2\pi]$.

274 The expression of \bar{p} in (10) is complex and can be calculated
 275 numerically. However, it is not tractable to obtain in closed-
 276 form expression, except for the deterministic channel when
 277 $\beta = 2$. Therefore, an upper bound expression for \bar{p} , denoted
 278 by \bar{p}_{up} , should be derived in closed-form for UCA in order
 279 to facilitate detailed theoretical analysis. Notice that for other
 280 array types, the method of analyzing \bar{p} via closed-form expres-
 281 sion of \bar{p}_{up} still works. If closed-form expressions of \bar{p}_{up} do
 282 not exist, appropriate approximations or numerical results can
 283 be used based on the particular form of given $G(\theta, \theta_B)$.

284 III. CLOSED-FORM EXPRESSION FOR 285 THE UPPER BOUND FOR SSOP

286 A. Derivation of the Upper Bound for UCA

287 Firstly, a general upper bound is briefly introduced as
 288 follows, based on which the particular upper bound for UCA
 289 can be derived. For a given λ_e and K , \bar{p}_{up} can be derived
 290 using Jensen's inequality.

$$291 \bar{p}_{up} = 1 - \exp\left\{-\lambda_e \pi \left[c_0 P_t \frac{K A_0 + 2\pi}{2\pi(K+1)} \right]^{\frac{2}{\beta}}\right\}, \quad (12)$$

292 where A_0 denotes the pattern area and is given by,

$$293 A_0 = \int_0^{2\pi} G^2(\theta, \theta_B) d\theta. \quad (13)$$

294 The derivation is described in [19]. According to (12), \bar{p}_{up} is
 295 monotonically increasing with A_0 for any K and β . Therefore,
 296 \bar{p}_{up} can be analyzed via A_0 .

297 Notice that the expression of A_0 in (13) contains $G(\theta, \theta_B)$
 298 which is a general expression. To obtain the particular expres-
 299 sion for the UCA, the expression of A_0 needs to be determined.
 300 We can isolate θ to solve the integral in (4).

$$301 G^2(\theta, \theta_B) = \frac{1}{N} \sum_{i,j} e^{jkR[\cos(\theta_B - \psi_i) - \cos(\theta_B - \psi_j)]} \\ 302 \cdot e^{-jkR[\cos(\theta - \psi_i) - \cos(\theta - \psi_j)]}, \quad (14)$$

where $\sum_{i,j}$ represents $\sum_{i=1}^N \sum_{j=1}^N$ and $\cos(\theta - \psi_i) -$
 303 $\cos(\theta - \psi_j)$ can be further derived by 304

$$305 \cos(\theta - \psi_i) - \cos(\theta - \psi_j) = 2 \sin\left(\theta - \frac{i+j-2}{N}\pi\right) \sin\left(\frac{i-j}{N}\pi\right). \quad (15) \quad 306$$

Let $W_{i,j} = 2 \sin(\frac{i-j}{N}\pi)$ and $Z_{i,j} = \frac{i+j-2}{N}\pi$. Substituting (15)
 307 into (14), $G^2(\theta, \theta_B)$ can be derived as 308

$$309 \frac{1}{N} \sum_{i,j} e^{jkRW_{i,j} \sin(\theta_B - Z_{i,j})} \cdot e^{-jkRW_{i,j} \sin(\theta - Z_{i,j})}. \quad (16)$$

According to $J_n(x) = \frac{1}{2\pi} \int_{-\pi}^{\pi} e^{j(n\tau - x \sin \tau)} d\tau$, where $J_n(x)$ is
 310 the Bessel function of the first kind with order n , the following
 311 integration can be derived. 312

$$\int_0^{2\pi} e^{-jkRW_{i,j} \sin(\theta - Z_{i,j})} d\theta \\ 313 = \int_{-Z_{i,j}}^{2\pi - Z_{i,j}} e^{j[0\cdot\tau - kRW_{i,j} \sin \tau]} d(\tau + Z_{i,j}) \\ 314 = \int_{-\pi}^{\pi} e^{j[0\cdot\theta - kRW_{i,j} \sin \tau]} d\tau = 2\pi J_0(kRW_{i,j}) \quad (17) \quad 315$$

Note that in the second step, the upper and lower limits can be
 316 transformed to π and $-\pi$, because $\sin \tau$ is a periodic function
 317 with a period of 2π . 318

Combining (16) and (17), A_0 in (13) can be written as 319

$$320 A_0 = \frac{2\pi}{N} \sum_{i,j} J_0(kRW_{i,j}) e^{jkRW_{i,j} \sin(\theta_B - Z_{i,j})}. \quad (18)$$

The double summation of Bessel functions in (18) is
 321 intractable to analyze. In the following, A_0 will be further
 322 simplified. Let $A_{0,i,j}$ denote each summation term in (18), 323

$$324 A_{0,i,j} = \frac{2\pi}{N} J_0(kRW_{i,j}) e^{jkRW_{i,j} \sin(\theta_B - Z_{i,j})}. \quad (19) \quad 325$$

It is deduced that $W_{i,j} = -W_{j,i}$ and $Z_{i,j} = Z_{j,i}$. Considering
 326 that $J_n(-x) = (-1)^n J_n(x)$ and $J_0(x)$ is a real number, it can
 327 be deduced that $A_{0,i,j} = A_{0,j,i}^*$. In addition, it can be shown
 328 from the expression of $W_{i,j}$ and $Z_{i,j}$ that $W_{i,j+N} = -W_{i,j}$.
 329 Similarly, $\sin(\theta_B - Z_{i,j+N}) = -\sin(\theta_B - Z_{i,j})$. Thus, it can
 330 be determined found that $A_{0,i,j} = A_{0,i,j+N}$.

A table of $A_{0,i,j}$ is shown in Fig.3 to illustrate how to
 331 use the previous properties to simplify the summation of A_0
 332 in (18). For $N = 4$, the table is extended to $j = 8$. As $A_{0,i,j} =$
 333 $A_{0,i,j+N}$, the blue region is equivalent to the green region.
 334 Instead of adding $A_{i,j}$ for i, j from 1 to N , the summation
 335 can now be executed diagonally. For convenience, let $n = i - j$.
 336 Then, $W_n = W_{i,j} = 2 \sin(\frac{n}{N}\pi)$. The terms $A_{0,i,j}$ on the red
 337 diagonal lines in the table have the same W_n . In the table,
 338 $\frac{N}{\pi} Z_{i,j}$ is allocated according to their indices i and j . Given
 339 $n = i - j$, it can be derived that 340

$$341 Z_{n,i} = Z_{i,j} = \frac{i+j-2}{N}\pi = \frac{2i-n-2}{N}\pi. \quad (20)$$

Thus, it can be derived that 342

$$343 A_{0,n,i} = A_{0,i,j} = \frac{2\pi}{N} J_0(kRW_n) e^{jkRW_n \sin(\theta_B - Z_{n,i})}. \quad (21) \quad 344$$

| | | $\frac{N}{\pi}Z_{i,j} = i+j-2$ | | | | | | | | |
|-----------------|---|--------------------------------|---|-------|------------------------|--------|--------|--------|--|--|
| $i \setminus j$ | 1 | 2 | 3 | 4 | 5 | 6 | 7 | 8 | | |
| 1 | 0 | 1 | 2 | 3 | extened table: $j > 4$ | | | | | |
| 2 | 1 | 2 | 3 | 4 | 5 | | | | | |
| 3 | 2 | 3 | 4 | 5 | 6 | 7 | | | | |
| 4 | 3 | 4 | 5 | 6 | 7 | 8 | 9 | | | |
| $n=i-j$ | | | | $n=0$ | | $n=-1$ | $n=-2$ | $n=-3$ | | |

 Fig. 3. Table for $Z_{i,j}$, $N = 4$.

A_0 is the summation of all elements in the original table (i.e., $i, j = 1, \dots, 4$). Because $A_{0,i,j+N} = A_{0,i,j}$, the calculation of A_0 can be executed by replacing the lower triangle in the original table (i.e., $i > j$) with the lower triangle in the extended table (i.e., $i > j - N$). In the new formation of A_0 , which is a parallelogram table, the summation can be carried out along the diagonal lines from $n = 0$ to $n = -(N - 1)$. For any n , the summation of $A_{0,n,i}$ includes N terms with $Z_{n,i}$. Thus, (18) can be converted into

$$\begin{aligned}
 A_0 &= \sum_{i=1}^N \sum_{j=1}^N A_{0,i,j} = \sum_{n=0}^{-(N-1)} \sum_{i=1}^N A_{0,n,i} \\
 &= \sum_{n=0}^{-(N-1)} \sum_{i=1}^N \frac{2\pi}{N} J_0(kRW_n) e^{jkRW_n \sin(\theta_B - Z_{n,i})} \\
 &= \frac{2\pi}{N} \sum_{n=0}^{-(N-1)} J_0(kRW_n) \sum_{i=1}^N e^{jkRW_n \sin(\theta_B - Z_{n,i})}. \quad (22)
 \end{aligned}$$

According to Jacobi-Anger expansion $e^{ja \sin \gamma} = \sum_{m=-\infty}^{\infty} J_m(\alpha) e^{jm\gamma}$, (22) can be further derived by (23) at the bottom of the following page.

When $m = lN$, $l \in \mathbb{Z}$, $e^{j\pi \frac{m}{N}(n+2)} = e^{jlN\pi} e^{j2\pi l} = e^{jlN\pi}$ and

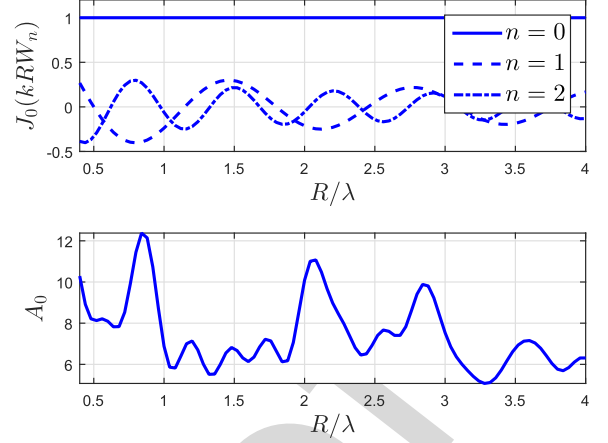
$$\sum_{i=1}^N e^{-j2\pi \frac{m}{N}i} = \sum_{i=1}^N e^{-j2\pi li} = N. \quad (24)$$

When $m \neq lN$,

$$\sum_{i=1}^N e^{-j2\pi \frac{m}{N}i} = e^{-j2\pi \frac{m}{N}} \frac{1 - e^{-j2\pi \frac{m}{N}N}}{1 - e^{-j2\pi \frac{m}{N}}} = 0. \quad (25)$$

Thus, it can be derived that

$$\begin{aligned}
 A_0 &= \frac{2\pi}{N} \sum_{n=0}^{-(N-1)} J_0(kRW_n) \sum_{l=-\infty}^{\infty} J_{lN}(kRW_n) e^{jlN\theta_B} e^{jlN\pi} \\
 &= 2\pi \sum_{n=0}^{-(N-1)} J_0(kRW_n) \sum_{l=-\infty}^{\infty} J_{lN}(kRW_n) e^{jlN\theta_B} (-1)^{ln} \\
 &= 2\pi \sum_{n=0}^{N-1} J_0(-kRW_n) \sum_{l=-\infty}^{\infty} (-1)^{-ln} J_{lN}(-kRW_n) e^{jlN\theta_B} \\
 &= 2\pi \sum_{n=0}^{N-1} J_0(kRW_n) \sum_{l=-\infty}^{\infty} (-1)^{ln+lN} J_{lN}(kRW_n) e^{jlN\theta_B}. \quad (26)
 \end{aligned}$$


 Fig. 4. Upper plot: Examples of $J_0(kRW_n)$ versus R . Lower plot: A_0 versus R . $N = 8$, $\theta_B = 0^\circ$.

Substituting (26) in (13), the closed-form expression for \bar{p}_{up} in (12) can be obtained. Compared to (13), the expression of A_0 in (26) consists of a finite summation of $J_0(\cdot)$ and an infinite summation of $J_{lN}(\cdot)$, which can provide asymptotic analysis.

B. Impact of R on A_0

As discussed in Section II-C, the impact of R will be used as a starting point to formulate the optimization problem. In the low region of x , the Bessel function $J_{lN}(x)$ in (26) is negligible for high order lN , i.e., $lN \gg 1$. Let x_0 denote the upper limit of the range $x \in [0, x_0]$ where $J_{lN}(x)$ is negligible for certain lN . Then, the specific value x_0 depends on the order lN . As the order lN increases, x_0 increases and eventually exceeds the value of $2kR$, which is the upper limit of $x = KRW_n$ in (26) for a fixed R . Once x_0 becomes larger than $2kR$, all $J_{lN}(x)$ for $l \geq 1$ are negligible in the range $(0, 2kR]$. Thus, for sufficiently large N , A_0 in (26) can be approximated by

$$A_0 \approx 2\pi \sum_{n=0}^{N-1} J_0^2(kRW_n). \quad (27)$$

The asymptotic behavior of A_0 versus R can be analyzed through (27). As shown in the upper plot in Fig.4, when $n = 0$, $J_0(kRW_0) = 1$, because $W_0 = 0$ and $J_0(0)$ is a constant that is irrelevant to R . When $n \neq 0$, $J_0(kRW_n)$ gradually decreases with some fluctuation as R increases, which is determined by the nature of $J_0(\cdot)$. Notice that in the asymptotic expression in (27), the angle θ_B is neglected. When N is not large enough, the term $J_{lN}(kRW_n) e^{jlN\theta_B}$ also needs to be considered. As $J_n(x)$ decreases and approaches zero with different convergence speed, the summation of a series of Bessel functions, i.e., A_0 , in general decreases and approaches a certain value as R increases. Due to the difference in the converging speed of $J_{lN}(kRW_n)$, there are some fluctuations.

An example of A_0 versus R is shown in the lower plot in Fig.4 where $N = 8$ and $\theta_B = 0^\circ$. It can be seen that A_0 fluctuates as R increases, because the curve is a superposition of $J_{lN}(kRW_n)$ with different orders lN . Thus,

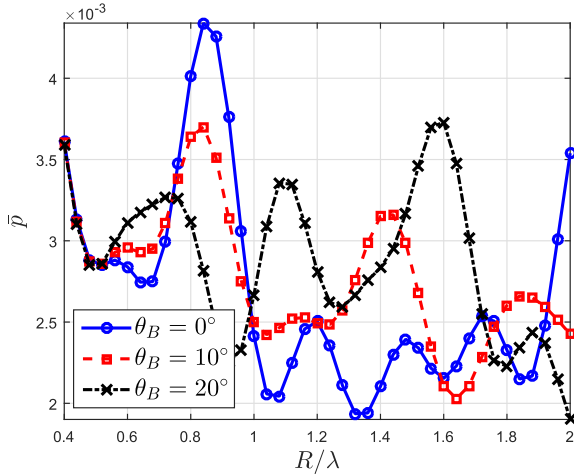


Fig. 5. \bar{p} versus R for different values of θ_B , $N = 8$, $P_t/\sigma_n^2 = 15$ dB, $R_B = 3.4594$ bps/Hz, $R_s = 1$ bps/Hz, $\lambda_e = 1 \times 10^{-4}$.

in a local region, e.g., $R < 2\lambda$, the minimum value does not necessarily correspond to a large or small R , which leads to the optimization problem for R .

IV. OPTIMIZATION ALGORITHM

A. Refined Optimization Problem

As mentioned in Section III-B, R can be properly designed according to θ_B to achieve a local minimum value in a certain range of R . According to Section II-C, d_B is not involved in the expression of \bar{p} . Thus, the optimization problem can be solved by optimizing R according to θ_B .

It is worth noticing that although the closed-form expression of \bar{p}_{up} provides an asymptotic analysis on the impact of R , it does not provide accurate results for the optimum value for R . As it is intractable to analyze the expression of \bar{p} in (10), we will use numerical results to determine this.

Examples of \bar{p} versus R for different θ_B are shown in Fig. 5 where $N = 8$. For simplicity, let $K \rightarrow \infty$ and $\beta = 2$, i.e., the channel is degraded to a free-space channel. More results for Rician fading channel will be provided in Section V-A. For the purpose of MATLAB simulation, the value of R is taken by a step of 1 cm in the range $[0.4\lambda, 2\lambda]$. Typical values of θ_B , i.e., $\theta_B = 0^\circ, 10^\circ, 20^\circ$, are taken for the UCA with $N = 8$. Fig. 5 depicts the fluctuating behavior of \bar{p} with respect to R for different values of θ_B . It can be seen that the curves for different θ_B vary. Therefore, for each θ_B , the local minimum of \bar{p} in the range $R \in [0.4\lambda, 2\lambda]$ is given by a different value of R . This suggests that by varying θ_B , a different R should be chosen in order to achieve a minimum \bar{p} . However, this is

not practical because R is usually predefined for an existing UCA.

Since R can only be a particular value, the optimum value R_{opt} needs to be pre-designed. To this end, the minimum mean error is used to find R_{opt} in a certain range of R that produces the minimum \bar{p} for all possible $\theta_B \sim \mathcal{U}(0, 2\pi)$. To establish the cost function, imagine that R is adjustable, which provides the hypothetical function of \bar{p}_{min} with respect to θ_B . Notice that the value of \bar{p}_{min} for each θ_B is, in fact, given by a different value of R . To find R_{opt} , let the mean error, denoted by $err(R)$, be the mean value of the difference between \bar{p} and \bar{p}_{min} over the range $\theta_B \in [0, 2\pi]$,

$$err(R) = \mathbb{E}_{\theta_B}[\bar{p} - \bar{p}_{min}]. \quad (28)$$

Note that the mean error is used instead of the mean square error because $\bar{p} - \bar{p}_{min}$ is always non-negative. Thus, R_{opt} can be found by

$$R_{opt} = \arg \min_R err(R). \quad (29)$$

(29) can be converted into the following expression, the derivation of which is in Appendix A.

$$R_{opt} = \arg \min_R \bar{\bar{p}}, \quad (30)$$

where $\bar{\bar{p}}$ is the averaged \bar{p} over Bob's angles and is defined by

$$\bar{\bar{p}} = \frac{1}{2\pi} \int_0^{2\pi} \bar{p} d\theta_B. \quad (31)$$

B. Analysis and Implementation of Optimization Algorithm

Substituting the expression of \bar{p} in (10) into (31), the expression of $\bar{\bar{p}}$ can be obtained,

$$\begin{aligned} \bar{\bar{p}} = & 1 - \frac{1}{2\pi} \int_{-\infty}^{\infty} \int_{-\infty}^{\infty} \int_0^{2\pi} \exp\left\{-\frac{\lambda_e}{2}(c_0 P_t)^{\frac{2}{\beta}}\right. \\ & \times \int_0^{2\pi} \left[\frac{K G_C^2(\theta, \theta_B)}{K+1} + \frac{x^2 + y^2}{K+1}\right. \\ & \left. \left. + \frac{2\sqrt{K} G_C(\theta, \theta_B)}{K+1} x\right]^{\frac{2}{\beta}} d\theta\right\} \frac{e^{-(x^2+y^2)}}{\pi} d\theta_B dx dy. \end{aligned} \quad (32)$$

Although (32) can be numerically calculated, it is intractable to analyze. Thus, the upper bound, denoted by $\bar{\bar{p}}_{up}$, is required for theoretical analysis.

Theorem 1:

$$\bar{\bar{p}}_{up} = 1 - \exp\left\{-\lambda_e \pi \left[\frac{c_0 K \bar{A}_0}{2\pi(K+1)} + \frac{c_0}{K+1}\right]^{\frac{2}{\beta}}\right\}, \quad (33)$$

where \bar{A}_0 is the expectation of A_0 over θ_B and is given by

$$\bar{A}_0 = \frac{1}{2\pi} \int_0^{2\pi} A_0 d\theta_B = 2\pi \sum_{n=0}^{N-1} J_0^2(kRW_n). \quad (34)$$

$$\begin{aligned} A_0 &= \frac{2\pi}{N} \sum_{n=0}^{-(N-1)} J_0(kRW_n) \sum_{i=1}^N \sum_{m=-\infty}^{\infty} J_m(kRW_n) e^{jm(\theta_B - Z_{n,i})} = \frac{2\pi}{N} \sum_{n=0}^{-(N-1)} J_0(kRW_n) \sum_{m=-\infty}^{\infty} J_m(kRW_n) e^{jm\theta_B} \sum_{i=1}^N e^{-jmZ_{n,i}} \\ &= \frac{2\pi}{N} \sum_{n=0}^{-(N-1)} J_0(kRW_n) \sum_{m=-\infty}^{\infty} J_m(kRW_n) e^{jm\theta_B} e^{j\pi \frac{m}{N}(n+2)} \sum_{i=1}^N e^{-j2\pi \frac{m}{N}i}. \end{aligned} \quad (23)$$

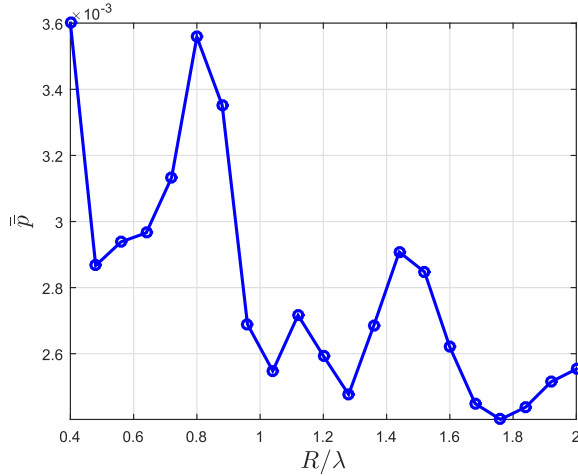


Fig. 6. \bar{p} versus R for all θ_B , $N = 8$, $P_t/\sigma_n^2 = 15$ dB, $R_B = 3.4594$ bps/Hz, $R_S = 1$ bps/Hz, $\lambda_e = 1 \times 10^{-4}$.

469 The proof of Theorem 1 is given in Appendix B. It can be seen
 470 that (34) has a similar composition to A_0 in (26). Therefore,
 471 \bar{A}_0 in general decreases with some fluctuations as R increases.
 472 Due to the monotonically increasing relationship between \bar{p}_{up}
 473 and \bar{A}_0 , it can be deduced that \bar{p} decreases in general with
 474 some fluctuations as R increases.

475 Because \bar{p} fluctuates in a certain range of R , there must
 476 exist at least one local minimum. Numerical results are used
 477 to find R_{opt} in (30). For example, choosing $N = 8$ and
 478 $R \in [0.4\lambda, 2\lambda]$, the results of \bar{p} shown in Fig. 6 are obtained
 479 where the channel is chosen as a free-space channel. It can
 480 be seen that there is more than one local minimum. In the
 481 range $R \in [0.4\lambda, 2\lambda]$, $R_{opt} = 1.76\lambda$ gives the minimum \bar{p}
 482 as 2.4×10^{-3} . Compared to the maximum value of \bar{p} that is
 483 3.6×10^{-3} in the same range, there is a 33% reduction in
 484 the value of \bar{p} . This indicates that by choosing an appropriate
 485 value of R , the averaged SSOP can be dramatically reduced.

486 The numerical implementation of the algorithm is shown in
 487 Algorithm 1. The continuous ranges of R , θ_B , θ are discretized
 488 with steps of ΔR , $\Delta\theta_B$ and $\Delta\theta$, respectively. In addition,
 489 a limit value Q is used when calculating integral from $-\infty$
 490 to ∞ in (32). For a normal distribution, a realistic value is set
 491 for Q , namely 3. Let N_R , N_{θ_B} , N_{θ} and N_Q be the number of
 492 samples for R , θ_B , θ and the integration range Q respectively,
 493 which determines the iteration numbers.

494 There are two main steps in the optimization algorithm.
 495 The first step is from line 3 to 15, where \bar{p} for a range of
 496 discretized R is calculated. Notice that the integrals in (32)
 497 are implemented via iterated summation from line 6 to 15. The
 498 second step section is from line 16 to 21, where the minimum
 499 value \bar{p}_{min} in the vector \bar{p} is searched to find R_{opt} which is
 500 the output of the optimization algorithm.

501 The accuracy of the result increases with number of sam-
 502 ples; however, the computational complexity also increases.
 503 The running time of the numerical implementation is approxi-
 504 mately $O(N_R N_{\theta_B} N_Q^2 N_{\theta})$. There is no specific restriction on the
 505 sampling interval as long as the chosen resolution generates a
 506 reasonable value.

Algorithm 1 Optimization of R for Fixed N .

INPUT: σ_n^2 , β , K , R_B , R_S , λ_e , λ , P_t , N

INPUT: R_1 , R_2 , ΔR ; θ_{B1} , θ_{B2} , $\Delta\theta_B$; θ_1 , θ_2 , $\Delta\theta$; Q , ΔQ

OUTPUT: R_{opt}

```

1: discretize  $R$ ,  $\theta_B$ ,  $\theta$ ,  $Q$ 
2: calculate  $N_R$ ,  $N_{\theta_B}$ ,  $N_{\theta}$ ,  $N_Q$  and  $c_0$ 
3: create an  $1 \times N_R$  empty vector of  $\bar{p}$  with index  $idx$ 
4: for each value of  $R \in [R_1, R_2]$ ,  $\theta_B \in [\theta_{B1}, \theta_{B2}]$  do
5:    $S_1 = 0$ 
6:   for each value of  $x, y \in [-Q, Q]$  do
7:      $S_2 = 0$ 
8:     for each value of  $\theta \in [\theta_1, \theta_2]$  do
9:        $S_2 = S_2 +$ 
10:         $\left[ \frac{KG^2(\theta, \theta_B) + x^2 + y^2 + 2\sqrt{K}G(\theta, \theta_B)xy}{K+1} \right]^{\frac{2}{\beta}} \Delta\theta$ 
11:     end for
12:      $S_1 = S_1 + \exp\left\{-\frac{\lambda_e}{2}(P_t c_0)^{\frac{2}{\beta}} S_2\right\} \frac{e^{-(x^2+y^2)}}{\pi} \Delta Q^2$ 
13:   end for
14:    $\bar{p}(idx) = \bar{p}(idx) + (1 - S_1)/N_{\theta_B}$ 
15: end for
16: initialization:  $R_{opt} = R_1$ ,  $\bar{p}_{min} = \bar{p}(1)$ 
17: for each value of  $R \in [R_1, R_2]$  do
18:   if  $\bar{p}_{min} > \bar{p}(idx)$  then
19:     reassignment:  $R_{opt} = R$ ,  $\bar{p}_{min} = \bar{p}(idx)$ 
20:   end if
21: end for

```

V. SIMULATION AND NUMERICAL RESULTS

507 In this section, we first provide simulation results for \bar{p}
 508 in (10) and then numerical results for \bar{p} in (32) over the Rician
 509 channel with a wider range of values of K and β . Next, the
 510 numerical results of the upper bounds \bar{p}_{up} and \bar{p}_{up} are shown
 511 in comparison with \bar{p} and \bar{p} to demonstrate the validity of the
 512 upper bounds. In the end, we investigate a common problem
 513 in antenna array, i.e., the mutual coupling and its effect on \bar{p} .
 514

A. More Results for Rician Fading Channels

515 In Section IV-B, numerical results are used to show the
 516 properties of \bar{p} versus R . Firstly, the simulation results are
 517 provided to validate the expressions of \bar{p} in (10) that is derived
 518 from the expression in (9) which contains Gaussian random
 519 variables via $|\tilde{h}^2|$ according to (3). We choose $K = 10$ and
 520 $\beta = 3$ as an example to compare the numerical results based
 521 on the expression in (10) and the simulation results based
 522 on the expression in (9). We ran Monte Carlo simulations to
 523 generate 1×10^4 samples of g_{Re} and g_{Im} in (3). As stated in
 524 Section II-C, the noise variance σ_n^2 , channel factors β and K ,
 525 the security related parameters R_B and R_S and the density
 526 of Eves λ_e are assumed to be constant; the transmit power
 527 P_t does not affect the impact of the array parameters to the
 528 SSOP. In this section, P_t and σ_n^2 are set to -65 dBm and
 529 -80 dBm, respectively. The rate of the transmitted codewords
 530 R_B is set to 3.4594 bps/Hz which corresponds to a received
 531 SNR of 10 dB for Bob. The rate of the confidential information
 532 R_S is set to be smaller than R_B , e.g., 1 bps/Hz as used in [18].
 533 The density of Eves is set to 1×10^{-4} which means 100 Eves
 534

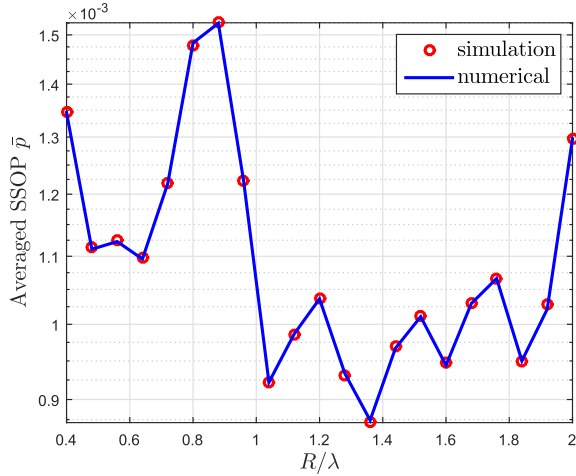


Fig. 7. Simulation and numerical results for \bar{p} versus R ; $K = 10$, $\beta = 3$, $\theta_B = 0^\circ$, $P_t/\sigma_n^2 = 15$ dB, $R_B = 3.4594$ bps/Hz, $R_s = 1$ bps/Hz, $\lambda_e = 1 \times 10^{-4}$.

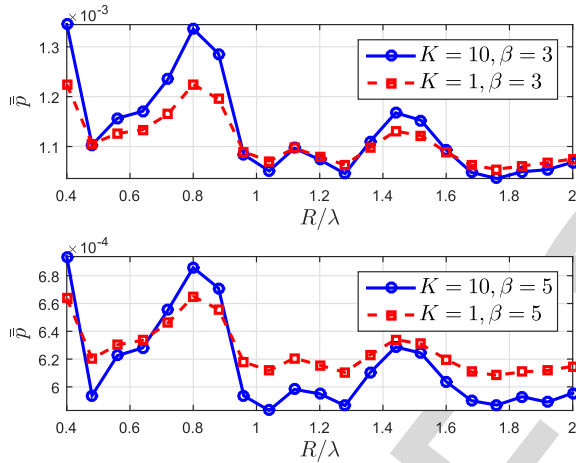


Fig. 8. Numerical results for \bar{p} versus R ; $P_t/\sigma_n^2 = 15$ dB, $R_B = 3.4594$ bps/Hz, $R_s = 1$ bps/Hz, $\lambda_e = 1 \times 10^{-4}$.

in 1000×1000 m². Finally, the radius of the UCA is set to $[0.4\lambda, 2\lambda]$, which corresponds to $[5, 25]$ cm for 2.4 GHz frequency. For comparison, a commercial uniform circular array FCI-3710 developed by Fidelity Comtech has 15.24 cm radius [29]. The simulation and numerical results plotted in Fig. 7 show a good match between them, which verifies the validity of the expressions in (10).

Secondly, a wider range of K and β for Rician channel will be examined. We choose typical value of $\beta = 3, 5$ and $K = 1, 10$. The results of \bar{p} is calculated according to (32). As shown in Fig. 8, all curves exhibit similar trend with regard to R to the curve in Fig. 6 where $K \rightarrow \infty$ and $\beta = 2$. In addition, for both curves in Fig. 8, the optimum value R_{opt} in the range $R \in [0.4\lambda, 2\lambda]$ is 1.76λ . It means that the optimum value of R in a certain range is valid for Rician channels with different K and β .

B. Numerical Results of the Upper Bounds

Next, closed-form expressions of \bar{p}_{up} and $\bar{\bar{p}}_{up}$ are derived in Section III-A and Section IV-B, respectively, in order to facilitate analysis. Here, some numerical results are shown to

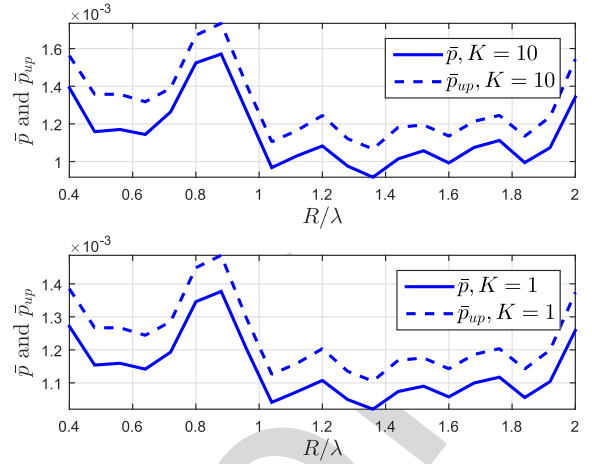


Fig. 9. Numerical results for \bar{p} and \bar{p}_{up} versus R ; $\beta = 3$, $P_t/\sigma_n^2 = 15$ dB, $R_B = 3.4594$ bps/Hz, $R_s = 1$ bps/Hz, $\lambda_e = 1 \times 10^{-4}$.

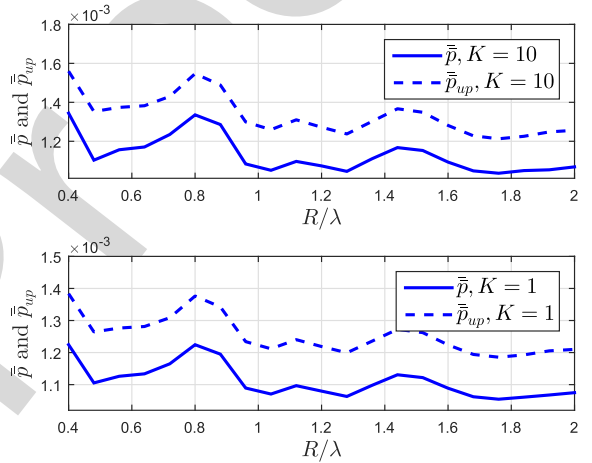


Fig. 10. Numerical results for \bar{p} and \bar{p}_{up} versus R ; $\beta = 3$, $P_t/\sigma_n^2 = 15$ dB, $R_B = 3.4594$ bps/Hz, $R_s = 1$ bps/Hz, $\lambda_e = 1 \times 10^{-4}$.

demonstrate that the upper bounds can reflect the fluctuating behavior of \bar{p} and $\bar{\bar{p}}$ against R .

In Fig. 9, the results for \bar{p} and \bar{p}_{up} versus R are shown for typical values of $\beta = 3$ and $K = 1, 10$. It can be seen that the curves of \bar{p}_{up} have a similar shape to the curves of \bar{p} , and the value of \bar{p}_{up} is close to \bar{p} . This suggests that the upper bound can very well reflect the property of \bar{p} .

In Fig. 10, the results for \bar{p} and \bar{p}_{up} versus R are shown for typical values of $\beta = 3$ and $K = 1, 10$. It can be seen that the curves for \bar{p} and \bar{p}_{up} have a similar shape, and the values of \bar{p} and \bar{p}_{up} are close to each other, which means that \bar{p}_{up} is a good upper bound.

C. Impact of Mutual Coupling

The mutual coupling is caused by energy absorption between proximate antennas and causes distortion to the array factor $G(\theta, \theta_B)$, and thus affects \bar{p} and the optimization algorithm. In this paper, we choose the NEC tool [26] to build a numerical model as an example to examine the impact of the mutual coupling, although any analytical model will apply.

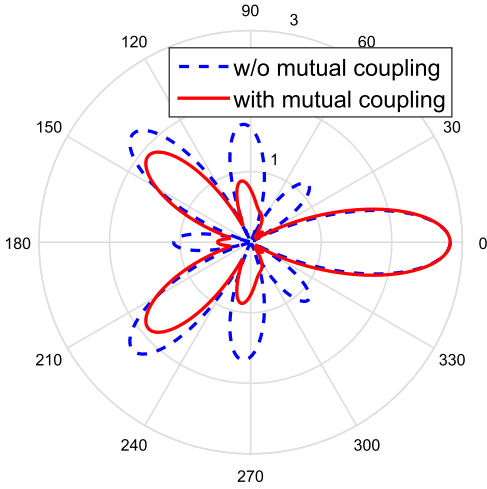


Fig. 11. Example of theoretical and NEC simulated patterns, $N = 8$, $R = 0.8\lambda$, $\theta_B = 0^\circ$.

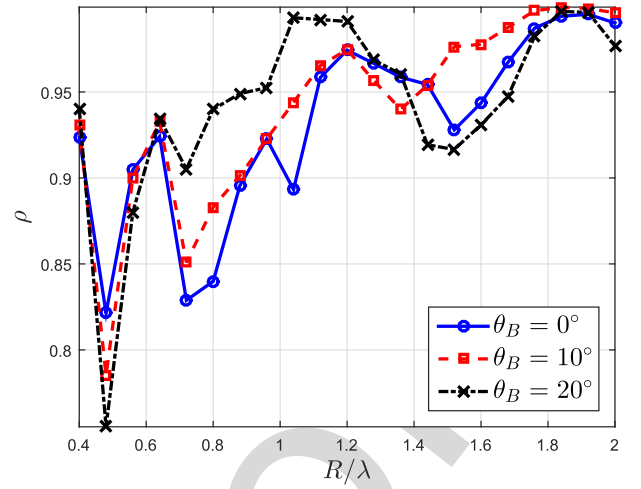


Fig. 12. Correlation coefficients between theoretical and NEC simulated patterns, $N = 8$, $P_t/\sigma_n^2 = 15$ dB, $R_B = 3.4594$ bps/Hz, $R_s = 1$ bps/Hz, $\lambda_e = 1 \times 10^{-4}$.

574 The NEC tool serves as a numerical method to calculate array pat-
 575 terns that include the mutual coupling effect, and its results
 576 are well accepted in the literature [30], [31].

577 An example shown in Fig. 11 illustrates the difference
 578 caused by the mutual coupling for system configurations with
 579 $N = 8$, $R = 0.8\lambda$, $\theta_B = 0^\circ$. The array pattern with the mutual
 580 coupling is calculated by the NEC simulation. It can be seen
 581 that there is not much difference in the main beam, but with
 582 deviation in the sidelobes.

583 To measure the array pattern distortion caused by the mutual
 584 coupling, Pearson's correlation coefficient, denoted by ρ ,
 585 is adopted. It measures the correlation between two variables
 586 X and Y , as defined by

$$\rho = \frac{\text{cov}(X, Y)}{\text{std}(X) \cdot \text{std}(Y)}, \quad (35)$$

588 where $\text{cov}(\cdot, \cdot)$ stands for the covariance and $\text{std}(\cdot)$ the stan-
 589 dard deviation. ρ between the theoretical array pattern and
 590 the simulated array pattern via NEC tool can be calculated to
 591 quantify their similarity. The larger ρ is, the more alike two
 592 patterns are.

593 The patterns of the UCA with a range of radius are
 594 simulated in NEC. For $N = 8$, typical values are chosen, i.e.,
 595 $\theta_B = 0^\circ, 10^\circ, 20^\circ$ in the range $R = [0.4\lambda, 2\lambda]$. The correlation
 596 coefficient, ρ , between the theoretical and NEC patterns is
 597 calculated and the results are shown in Fig. 12. It can be seen
 598 that ρ is generally above 0.8 in the range of $R = [0.4\lambda, 2\lambda]$,
 599 except for $R = 0.48\lambda$. This shows that the mutual coupling
 600 does not cause a significant distortion to the pattern of UCA.
 601 The high correlation between the theoretical and NEC patterns
 602 indicates that the optimization algorithm, which is based on
 603 empirical results on the theoretical patterns, can still work
 604 when considering the mutual coupling.

605 On the other hand, there exists some differences between the
 606 theoretical and NEC patterns, which means that when calculat-
 607 ing R_{opt} in the numerical implementation of the optimization
 608 algorithm, the NEC simulation data instead of the theoretical
 609 data should be used. To compare with Fig. 5, the same array
 610 parameters are adopted, i.e., $N = 8$ and $R \in [0.4\lambda, 2\lambda]$,

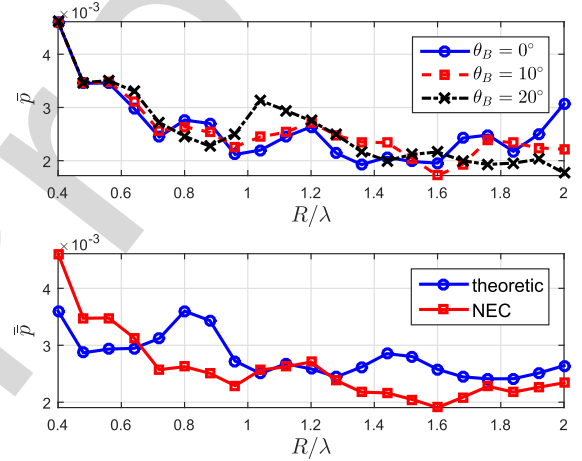


Fig. 13. Upper plot: $\bar{\rho}$ versus R . Lower plot: $\bar{\bar{\rho}}$ versus R . $N = 8$, $P_t/\sigma_n^2 = 15$ dB, $R_B = 3.4594$ bps/Hz, $R_s = 1$ bps/Hz, $\lambda_e = 1 \times 10^{-4}$.

611 and $\bar{\bar{\rho}}$ with the mutual coupling is calculated based on the
 612 NEC simulation data. The results are shown in the upper
 613 plot in Fig. 13. Compared to Fig. 5, it is not hard to notice
 614 the similarity between the theoretical and NEC simulated
 615 curves for the same θ_B , which can be explained by the high
 616 correlation between them, as shown in Fig. 12.

617 Because of the differences between the theoretical and
 618 NEC simulated results, $\bar{\bar{\rho}}$ in Fig. 6 needs to be re-calculated
 619 based on the NEC simulation data, in order to find R_{opt} . The
 620 lower plot in Fig. 13 shows $\bar{\bar{\rho}}$ based on the NEC simulation
 621 data in comparison with the theoretical curve. It can be
 622 seen that the optimum value for the NEC simulation data is
 623 $R_{opt} = 1.6\lambda$ compared to $R_{opt} = 1.76\lambda$ for the theoretical
 624 result. By choosing $R_{opt} = 1.6\lambda$, the value of $\bar{\bar{\rho}}$ is reduced
 625 dramatically by about 59% compared to the maximum value
 626 of $\bar{\bar{\rho}}$ at $R = 0.4\lambda$.

VI. CONCLUSIONS

627 This paper investigated the security performance of
 628 ER-based beamforming system with the UCA in the presence
 629 of PPP distributed Eves in Rician fading channel. With the aid
 630

of the expression of the averaged SSOP and the closed-form expression of its upper bound, an optimization algorithm with regard to the radius was developed to minimize the SSOP. This paper provides a mathematical relationship which allows the radius to be optimized for a given UCA with a certain number of elements. The optimization algorithm is still valid for mutual coupling in practice, however, the optimum value needs to be calculated based on the NEC simulation data. In this work, it is assumed that Bob's location is known by Alice beforehand. In practice, there could be inaccuracy in Bob's location information at Alice, whether Bob sends his location to Alice or Alice estimates Bob's location. In future work, it can be extended to include the impact of error in Bob's location when optimizing the array parameters in practice. We will also extend our work considering random locations of Bob.

APPENDIX A CONVERSION OF OPTIMIZATION PROBLEM

Because $\theta_B \sim \mathcal{U}(0, 2\pi)$, $\text{err}(R)$ can be calculated by

$$\text{err}(R) = \frac{1}{2\pi} \int_0^{2\pi} (\bar{p} - \bar{p}_{\min}) d\theta_B. \quad (36)$$

To find the minimum value of $\text{err}(R)$, the zeros of the partial derivative of $\text{err}(R)$ with respect to R are calculated,

$$\frac{\partial}{\partial R} \text{err}(R) = 0 \quad (37)$$

$$\Rightarrow \frac{\partial}{\partial R} \frac{1}{2\pi} \int_0^{2\pi} (\bar{p} - \bar{p}_{\min}) d\theta_B = 0 \quad (38)$$

$$\Rightarrow \frac{1}{2\pi} \int_0^{2\pi} \left(\frac{\partial}{\partial R} \bar{p} - \frac{\partial}{\partial R} \bar{p}_{\min} \right) d\theta_B = 0. \quad (39)$$

Because \bar{p}_{\min} is a fixed value for certain θ_B and only depends on θ_B , the partial derivative $\frac{\partial}{\partial R} \bar{p}_{\min} = 0$. Thus, it can be derived that

$$\frac{\partial}{\partial R} \text{err}(R) = 0 \quad (40)$$

$$\Rightarrow \frac{1}{2\pi} \int_0^{2\pi} \frac{\partial}{\partial R} \bar{p} d\theta_B = 0 \quad (41)$$

$$\Rightarrow \frac{\partial}{\partial R} \frac{1}{2\pi} \int_0^{2\pi} \bar{p} d\theta_B = 0 \quad (42)$$

$$\Rightarrow \frac{\partial}{\partial R} \bar{p} = 0, \quad (43)$$

where \bar{p} is the averaged SSOP over Bob's angle and is defined by

$$\bar{p} = \frac{1}{2\pi} \int_0^{2\pi} \bar{p} d\theta_B. \quad (44)$$

Thus, we can obtain

$$R_{opt} = \arg \min_R \bar{p}. \quad (45)$$

APPENDIX B PROOF OF THEOREM 1

To obtain the upper bound \bar{p}_{up} , two instances of Jensen's inequality will be used to derive \bar{p}_{up} .

$$\mathbb{E}[e^X] \geq e^{\mathbb{E}[X]}, \quad (46)$$

where X is a random variable. The equality holds if and only if X is a deterministic value. The other one involved is expressed by

$$\mathbb{E}[X^{\frac{2}{\beta}}] \leq (\mathbb{E}[X])^{\frac{2}{\beta}}, \quad (47)$$

where X is a random variable and $\beta \geq 2$. The equality holds when $\beta = 2$ for any X .

The upper bound \bar{p}_{up} can be derived based on $\bar{p} \leq \bar{p}_{up}$. Using (12), it can be derived that

$$\begin{aligned} \bar{p} &= \mathbb{E}_{\theta_B}[\bar{p}] \leq \mathbb{E}_{\theta_B}[\bar{p}_{up}] \\ &= 1 - \mathbb{E}_{\theta_B} \left[\exp \left\{ -\lambda_e \pi \left[\frac{c_0 K}{2\pi(K+1)} A_0 + \frac{c_0}{K+1} \right]^{\frac{2}{\beta}} \right\} \right]. \end{aligned} \quad (48)$$

Using (46) and (47), it can be derived that

$$1 - \mathbb{E}_{\theta_B} \left[\exp \left\{ -\lambda_e \pi \left[\frac{c_0 K}{2\pi(K+1)} A_0 + \frac{c_0}{K+1} \right]^{\frac{2}{\beta}} \right\} \right] \quad (49)$$

$$< 1 - \exp \left\{ -\lambda_e \pi \mathbb{E}_{\theta_B} \left[\left[\frac{c_0 K}{2\pi(K+1)} A_0 + \frac{c_0}{K+1} \right]^{\frac{2}{\beta}} \right] \right\} \quad (50)$$

$$\leq 1 - \exp \left\{ -\lambda_e \pi \left[\frac{c_0 K}{2\pi(K+1)} \mathbb{E}_{\theta_B}[A_0] + \frac{c_0}{K+1} \right]^{\frac{2}{\beta}} \right\}. \quad (51)$$

The equality in (50) does not hold because θ_B is random in this case. Then, \bar{p}_{up} can be obtained by

$$\bar{p}_{up} = 1 - \exp \left\{ -\lambda_e \pi \left[\frac{c_0 K \bar{A}_0}{2\pi(K+1)} + \frac{c_0}{K+1} \right]^{\frac{2}{\beta}} \right\}, \quad (52)$$

where \bar{A}_0 is the expectation of A_0 over θ_B and is given by

$$\bar{A}_0 = \mathbb{E}_{\theta_B}[A_0] = \frac{1}{2\pi} \int_0^{2\pi} A_0 d\theta_B. \quad (53)$$

The above equation can be calculated from (26) by directly solving the integral. Because

$$\int_0^{2\pi} e^{j l N \theta_B} d\theta_B = 0, \text{ for } l \neq 0 \quad (54)$$

it can be obtained that

$$\bar{A}_0 = 2\pi \sum_{n=0}^{N-1} J_0^2 \left(2kR \sin \left(\frac{n}{N} \pi \right) \right). \quad (55)$$

REFERENCES

- [1] A. Mukherjee, S. A. A. Fakoorian, J. Huang, and A. L. Swindlehurst, "Principles of physical layer security in multiuser wireless networks: A survey," *IEEE Commun. Surveys Tuts.*, vol. 16, no. 3, pp. 1550–1573, 3rd Quart., 2014.
- [2] Y. Liu, H.-H. Chen, and L. Wang, "Physical layer security for next generation wireless networks: Theories, technologies, and challenges," *IEEE Commun. Surveys Tuts.*, vol. 19, no. 1, pp. 347–376, 1st Quart., 2017.
- [3] A. D. Wyner, "The wire-tap channel," *Bell Syst. Tech. J.*, vol. 54, no. 8, pp. 1355–1387, 1975.

- 707 [4] J. Barros and M. R. Rodrigues, "Secrecy capacity of wireless channels,"
708 in *Proc. IEEE Int. Symp. Inf. Theory*, Jul. 2006, pp. 356–360. 783
- 709 [5] M. Bloch, J. Barros, M. R. D. Rodrigues, and S. W. McLaughlin, "Wire-
710 less information-theoretic security," *IEEE Trans. Inf. Theory*, vol. 54,
711 no. 6, pp. 2515–2534, Jun. 2008. 784
- 712 [6] S. Shafiee and S. Ulukus, "Achievable rates in Gaussian MISO channels
713 with secrecy constraints," in *Proc. IEEE ISIT*, Nice, France, Jun. 2007,
714 pp. 2466–2470. 785
- 715 [7] A. Khisti and G. W. Wornell, "Secure transmission with multiple
716 antennas I: The MISOME wiretap channel," *IEEE Trans. Inf. Theory*,
717 vol. 56, no. 7, pp. 3088–3104, Jul. 2010. 786
- 718 [8] A. Mukherjee and A. L. Swindlehurst, "Robust beamforming for security
719 in MIMO wiretap channels with imperfect CSI," *IEEE Trans. Signal
720 Process.*, vol. 59, no. 1, pp. 351–361, Jan. 2011. 787
- 721 [9] S. Yan and R. Malaney, "Location-based beamforming for enhancing
722 secrecy in rician wiretap channels," *IEEE Trans. Wireless Commun.*,
723 vol. 15, no. 4, pp. 2780–2791, Apr. 2016. 788
- 724 [10] S. Lakshmanan, C. L. Tsao, and R. Sivakumar, "Aegis: Physical space
725 security for wireless networks with smart antennas," *IEEE/ACM Trans.
726 Netw.*, vol. 18, no. 4, pp. 1105–1118, Aug. 2010. 789
- 727 [11] A. Sheth, S. Seshan, and D. Wetherall, "Geo-fencing: Confining Wi-Fi
728 coverage to physical boundaries," in *Proc. IEEE 7th Int. Conf. Pervasive
729 Comput.*, Nara, Japan, May 2009, pp. 274–290. 790
- 730 [12] N. Anand, S.-J. Lee, and E. W. Knightly, "STROBE: Actively securing
731 wireless communications using zero-forcing beamforming," in *Proc.
732 INFOCOM*, Mar. 2012, pp. 720–728. 791 AQ:4
- 733 [13] T. Wang and Y. Yang, "Enhancing wireless communication privacy with
734 artificial fading," in *Proc. IEEE 9th Int. Conf. Mobile Adhoc Sensor
735 Syst. (MASS)*, Oct. 2012, pp. 173–181.
- 736 [14] H. Li, X. Wang, and W. Hou, "Security enhancement in cooperative
737 jamming using compromised secrecy region minimization," in *Proc.
738 IEEE 13th Can. Workshop Inf. Theory*, Toronto, Canada, Jun. 2013,
739 pp. 214–218.
- 740 [15] J. Wang, J. Lee, F. Wang, and T. Q. Quek, "Jamming-aided secure com-
741 munication in massive MIMO Rician channels," *IEEE Trans. Wireless
742 Commun.*, vol. 14, no. 12, pp. 6854–6868, Dec. 2015.
- 743 [16] S. Sarma, S. Shukla, and J. Kuri, "Joint scheduling & jamming for data
744 secrecy in wireless networks," in *Proc. 11th Int. Symp. Modeling Optim.
745 Mobile, Ad Hoc Wireless Netw. (WiOpt)*, May 2013, pp. 248–255.
- 746 [17] W. Li, M. Ghogho, B. Chen, and C. Xiong, "Secure communi-
747 cation via sending artificial noise by the receiver: Outage secrecy
748 capacity/region analysis," *IEEE Commun. Lett.*, vol. 16, no. 10,
749 pp. 1628–1631, Oct. 2012.
- 750 [18] T.-X. Zheng, H.-M. Wang, and Q. Yin, "On transmission secrecy outage
751 of a multi-antenna system with randomly located eavesdroppers," *IEEE
752 Commun. Lett.*, vol. 18, no. 8, pp. 1299–1302, Aug. 2014.
- 753 [19] Y. Zhang, Y. Ko, R. Woods, and A. Marshall, "Defining spatial
754 secrecy outage probability for exposure region-based beamforming,"
755 *IEEE Trans. Wireless Commun.*, vol. 16, no. 2, pp. 900–912, Feb. 2017.
- 756 [20] B. Friedlander and A. J. Weiss, "Direction finding in the presence
757 of mutual coupling," *IEEE Trans. Antennas Propag.*, vol. 39, no. 3,
758 pp. 273–284, Mar. 1991.
- 759 [21] J. Dai, X. Bao, N. Hu, C. Chang, and W. Xu, "A recursive RARE
760 algorithm for DOA estimation with unknown mutual coupling," *IEEE
761 Antennas Wireless Propag. Lett.*, vol. 13, pp. 1593–1596, Aug. 2014.
- 762 [22] Y. Zhang, B. Yin, R. Woods, J. Cavallaro, A. Marshall, and Y. Ko,
763 "Investigation of secure wireless regions using configurable beamform-
764 ing on WARP," in *Proc. IEEE 48th Asilomar Conf. Signals, Syst.
765 Comput.*, Nov. 2014, pp. 1979–1983.
- 766 [23] B. Allen and M. Ghavami, *Adaptive Array Systems: Fundamentals and
767 Applications*. Hoboken, NJ, USA: Wiley, 2006.
- 768 [24] X. Zhou, M. R. McKay, B. Maham, and A. Hjørungnes, "Rethinking the
769 secrecy outage formulation: A secure transmission design perspective,"
770 *IEEE Commun. Lett.*, vol. 15, no. 3, pp. 302–304, Mar. 2011.
- 771 [25] Y. Zhang, Y. Ko, R. Woods, A. Marshall, J. Cavallaro, and K. Li, "On
772 spatial security outage probability derivation of exposure region based
773 beamforming with randomly located eavesdroppers," in *Proc. IEEE 50th
774 Asilomar Conf. Signals, Syst. Comput.*, Nov. 2016, pp. 689–690.
- 775 [26] G. J. Burke, A. J. Poggio, J. C. Logan, and J. W. Rockway, "Numerical
776 electromagnetic code (NEC)," in *Proc. IEEE Int. Symp. Electromagn.
777 Compat.*, Livermore, CA, USA, Oct. 1979, pp. 1–3.
- 778 [27] M. Ghogho and A. Swami, "Physical-layer secrecy of MIMO communi-
779 cations in the presence of a Poisson random field of eavesdroppers," in
780 *Proc. IEEE Int. Conf. Commun. (ICC)*, Kyoto, Japan, Jun. 2011, pp. 1–5.
- 781 [28] F. Gross, *Smart Antennas for Wireless Communications With MATLAB*.
782 New York, NY, USA: McGraw-Hill, 2005.
- [29] *FCI-3710 Phased Array Antenna*. Accessed: Oct. 25, 2017. 783
[Online]. Available: [http://www.fidelity-comtech.com/wp-content/
784 uploads/SpecSheet_FCI-3710.pdf](http://www.fidelity-comtech.com/wp-content/uploads/SpecSheet_FCI-3710.pdf) 785
- [30] K. R. Dandekar, H. Ling, and G. Xu, "Effect of mutual coupling on
786 direction finding in smart antenna applications," *Electron. Lett.*, vol. 36,
787 no. 22, pp. 1889–1891, Oct. 2000. 788
- [31] H. Singh, H. Sneha, and R. Jha, "Mutual coupling in phased
789 arrays: A review," *Int. J. Antennas Propag.*, vol. 2013, Mar. 2013,
790 Art. no. 348123. 791



Yuanrui Zhang received the B.Sc. degree in communication engineering from Shandong University, China, in 2009, the M.Sc. degree in communication and information technology from the University of Bremen, Germany, in 2012, and the Ph.D. degree in wireless innovation from Queen's University Belfast, U.K., in 2016. He is actively involved with areas in wireless communications, such as physical layer security, beamforming, and channel coding.



Roger Woods (M'95–SM'01) received the B.Sc. degree (Hons.) in electrical and electronic engineering and the Ph.D. degree from Queen's University Belfast in 1985 and 1990, respectively. He is currently a Full Professor with Queen's University Belfast, where he created and leads the Programmable Systems Laboratory. He has co-founded a spin-off company, Analytics Engines Ltd., which looks to exploit programmable systems research. His research interests are in heterogeneous programmable systems and system level design tools for data, signal and image processing, and telecommunications. He holds four patents and has authored over 200 papers. He is a member of the IEEE Signal Processing and Industrial Electronics Societies. He is on the Advisory Board for the IEEE SPS Technical Committee on the Design and Implementation of Signal Processing Systems. He is on the Editorial Board for the *ACM Transactions on Reconfigurable Technology and Systems*, the *Journal of VLSI Signal Processing Systems*, and the *IET Proceedings on Computer and Digital Techniques*. He was the General Chair for the 2014 Asilomar IEEE Conference on Signals, Systems, and Computers and is on the program committees of a number of IEEE conferences.



Youngwook Ko received the B.S.E. degree in information and communications engineering from Hannam University, South Korea, and the M.S. and Ph.D. degrees in electrical engineering from Arizona State University, Tempe, AZ, USA, in 2002 and 2006, respectively. He was with Samsung for two years, as a Senior Researcher. In 2008, he was with the Electrical and Computer Engineering Department, University of Alberta, Canada. From 2010 to 2013, he was with CCSR, University of Surrey, U.K., as a Senior Research Fellow. Since 2013, he has been with the ECIT Institute, Queen's University Belfast, as a Lecturer. He has authored over 40 publications in major IEEE international journals and peer-reviewed international conferences. He is a pioneer of index modulation techniques, and his current research include the areas of index modulation OFDM, sporadic machine type communications, physical wireless security, and the next generation wireless manufacturing systems. He was a recipient of several EPSRC and Newton projects, such as the EPSRC First Grant Award and the EPSRC IDS. He is a member of the EPSRC Peer-Review Associate College and is on the Editorial Board of the *Journal on Physical Communications* (Elsevier).

843
844
845
846
847
848
849
850
851
852
853
854
855
856
857
858
859
860
861
862
863
864



Alan Marshall (M'88–SM'00) has spent over 24 years of experience in the telecommunications and defense industries. He has been a Visiting Professor in network security with the University of Nice Sophia Antipolis/CNRS, France, and an Adjunct Professor of research with Sunway University Malaysia. He has authored over 200 scientific papers and holds a number of joint patents in the areas of communications and network security. His research interests include network architectures and protocols, mobile and wireless networks, network security, high-speed packet switching, quality of service and experience architectures, and distributed haptics. He is a fellow of the Institution of Engineering and Technology. He is currently the Chair in Communications Networks with the University of Liverpool, where he is also the Director of the Advanced Networks Group. He has formed a successful spin-out company, Traffic Observation & Management Ltd., specializing in intrusion detection and prevention for wireless networks. He is a Section Editor (section B: *Computer and Communications Networks and Systems*) for the *Computer Journal of the British Computer Society*, a member of the Editorial Board of the *Journal of Networks*, and on the program committees of a number of IEEE conferences.



Junqing Zhang received the B.Eng. and M.Eng. degrees in electrical engineering from Tianjin University, China, in 2009 and 2012, respectively, and the Ph.D. degree in electronics and electrical engineering from Queen's University Belfast, U.K., in 2016. He is currently a Post-Doctoral Research Fellow with Queen's University Belfast. His research interests include physical layer security and OFDM.

865
866
867
868
869
870
871
872

IEEE Proof

AUTHOR QUERIES

AUTHOR PLEASE ANSWER ALL QUERIES

PLEASE NOTE: We cannot accept new source files as corrections for your paper. If possible, please annotate the PDF proof we have sent you with your corrections and upload it via the Author Gateway. Alternatively, you may send us your corrections in list format. You may also upload revised graphics via the Author Gateway.

AQ:1 = Please be advised that per instructions from the Communications Society this proof was formatted in Times Roman font and therefore some of the fonts will appear different from the fonts in your originally submitted manuscript. For instance, the math calligraphy font may appear different due to usage of the usepackage[mathcal]euscript. We are no longer permitted to use Computer Modern fonts.

AQ:2 = Please note that there were discrepancies between the accepted pdf [single.pdf] and the [5 manuscript.tex] in the sentences on line nos 48 and 49. We have followed [5 manuscript.tex].

AQ:3 = Note that if you require corrections/changes to tables or figures, you must supply the revised files, as these items are not edited for you.

AQ:4 = Please confirm the volume no. for ref. [31].

Security Optimization of Exposure Region-Based Beamforming With a Uniform Circular Array

Yuanrui Zhang, Roger Woods¹, Senior Member, IEEE, Youngwook Ko,
Alan Marshall, Senior Member, IEEE, and Junqing Zhang²

Abstract—This paper investigates the impact of a uniform circular array (UCA) in the context of wireless security via exposure region-based beamforming. An improvement is demonstrated for the security metric proposed in our previous paper, namely, the spatial secrecy outage probability (SSOP), by optimizing the configuration of the UCA. Our previous paper focused on formalizing the SSOP concept and exploring its applicability using a uniform linear array example. This paper proposes the UCA as a superior candidate because it is more robust against the effects of mutual coupling. The UCA's SSOP configuration is explored and a special expression is derived from the general expression for the first time, and a closed-form upper bound is then generated to facilitate analysis. By carefully designing the UCA structure particularly the radius, an SSOP optimization algorithm is derived and explored for mutual coupling. It is shown that the information leakage to eavesdroppers is reduced while the legitimate user's received signal quality is enhanced due to the use of beamforming.

Index Terms—Physical layer security, beamforming, exposure region, spatial secrecy outage probability, uniform circular array.

I. INTRODUCTION

WIRELESS communication is vulnerable to passive eavesdropping due to its broadcast nature. Physical layer security exploits the unique and unpredictable features of wireless channels such as fading and has shown a great potential to secure future wireless technologies [1], [2]. This technique dates back to Wyner's seminal work on the wiretap channel model [3], which has triggered much fruitful research and has been extended to various channel models, such as fading channels and multiple antenna channels [4]–[7].

In the physical layer security scenario with legitimate users wishing to carry out secure communication with eavesdroppers

observing the transmissions, the channel of the legitimate user in Wyner's wiretap channel model is required to be better than that of the eavesdroppers, at least for a fraction of realizations in the case of fading channels [4]. When the legitimate transmitter is equipped with multiple antennas or an antenna array, beamforming is an effective technique to enlarge the difference of the legitimate users' and eavesdroppers' channel quality and can be achieved by exploiting the channel state information (CSI) [8] or the location information [9].

Beamforming can be used to create physical regions within which any user can correctly receive the message [10]–[13]; the area was defined as an 'exposure region' (ER) in [10]. However, these regions were not based on information-theoretic parameters, such as secrecy capacity or secrecy outage probability (SOP) [4], and thus lacked a quantitative measure of the security level. On the other hand, some information theoretical based methods lacked of the analysis from a physical perspective, for example, the aspect of antenna arrays [14]–[18].

In our previous work [19], we proposed an ER-based beamforming approach which led to the derivation of the spatial secrecy outage probability (SSOP) from an information-theoretic perspective and links with the antenna array configuration. Fig. 1 illustrates a transmitter (Alice) with an antenna array that communicates to a legitimate user (Bob) in the presence of eavesdroppers (Eves) with their location distribution following a Poisson point process (PPP); this hints towards the utilization of location in the Wyner's channel model. The ER is defined by the physical region where any PPP distributed Eve causes secrecy outage to the legitimate transmission in the Rician fading channel. In [19], the secrecy outage caused by PPP distributed Eves is quantitatively measured by the SSOP that is derived from the ER. The general expression of the SSOP for any type of array is derived and the uniform linear array (ULA) is used as an example to explore the properties of the array parameters.

Based on the knowledge of the previous work, we advance knowledge in this paper by optimizing the array parameters. The uniform circular array (UCA) is chosen rather than the ULA because of practical considerations, namely mutual coupling. Mutual coupling is the electromagnetic interaction between the antenna elements of an array and is always associated with multiple antenna techniques [20], [21]. In [22], it has been shown that linear arrays are susceptible to mutual coupling, thus rendering no effective optimum solution for

Manuscript received March 27, 2017; revised August 5, 2017 and September 27, 2017; accepted October 24, 2017. This work was supported by the US-Ireland R&D Partnership USI033 WiPhyLoc8 grant involving Rice University (USA), University College Dublin (Ireland) and Queen's University Belfast (Northern Ireland). The associate editor coordinating the review of this paper and approving it for publication was J. Yuan. (*Corresponding author: Roger Woods.*)

Y. Zhang, R. Woods, Y. Ko, and J. Zhang are with the School of Electronics, Electrical Engineering and Computer Science, Queen's University Belfast, Belfast BT9 5AH, U.K. (e-mail: yzhang31@qub.ac.uk; r.woods@qub.ac.uk; y.ko@qub.ac.uk; jzhang20@qub.ac.uk).

A. Marshall is with the Department of Electrical Engineering and Electronics, University of Liverpool, Liverpool L69 3GJ, U.K. (e-mail: alan.marshall@liverpool.ac.uk).

Color versions of one or more of the figures in this paper are available online at <http://ieeexplore.ieee.org>.

Digital Object Identifier 10.1109/TCOMM.2017.2768516

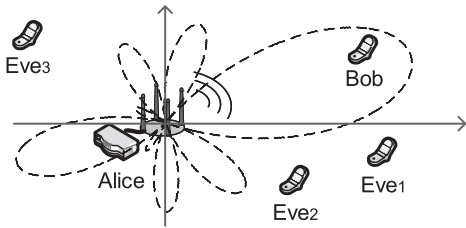


Fig. 1. The enclosed area surrounding Bob illustrates the ER created using a circular antenna array.

minimizing the SSOP. On the other hand, the UCA is less affected and produces a more symmetric beam pattern around 360° [23]. Thus, it is chosen as the candidate to exhibit the optimization of the array parameters, especially the radius.

We assume that Bob's location information is available at Alice, which is similar to that used in [9]. For example, Bob could send his own location information to Alice, if he wishes to be served by Alice with additional security features. Alice exploits Bob's location information to perform the beamforming.

In fading channels, the security performance of the aforementioned system, i.e., Alice using beamforming to enlarge the difference between Bob's and Eves' channels, can be expressed in terms of secrecy outage. In [24], the secrecy outage probability (SOP) for a single Eve is given by the probability that Eve's channel capacity is higher than a certain threshold; this is defined by the difference between the rate of the transmitted codewords and that of the confidential information, conditioned on Bob's channel capacity being larger than the rate of the transmitted codewords. In other words, the ER is an enclosed area within the boundary where Eve's channel capacity is just equal to that threshold. As Eve's channel capacity is random due to fading, the boundary of the ER shifts. In Fig. 1, the dashed curve depicts an ER boundary for a deterministic channel, which resembles the shape of the array pattern.

Intuitively, the smaller the ER is, the less possible that Eves are located inside the ER, and therefore the more secure the transmission will be. The overall secrecy outage caused by PPP distributed Eves, i.e., SSOP, is calculated with the aid of stochastic geometry theory, which links the security performance with the UCA parameters. This paper builds substantially on our previous work [19], [25] by investigating the SSOP with respect to UCA parameters in Rician fading channel and creating an optimization algorithm which minimizes the SSOP by adjusting the radius. In addition, the impact of mutual coupling is examined on the SSOP using a numerical simulation tool, i.e., NEC [26]. In essence, this sets the scene for setting secure regions in wireless networks. The main contributions of this paper are:

- Deriving the expression of the SSOP for the UCA and the closed-form expression of its upper bound for the first time, thus revealing the relationship between the security performance and various parameters, especially the radius of the UCA.
- Based on the expressions of the SSOP for the UCA, the first investigation of the security performance of

ER-based beamforming for a Rician fading channel with respect to radius is presented. Simulation and numerical results are covered, which show how the behavior of averaged SSOP varies with the radius.

- An optimization algorithm is derived based on the above analysis, which enhances the security level by optimizing the radius for all of Bob's possible angles. The impact of the mutual coupling with the radius is compared with the optimization algorithm and shows that while the algorithm in general is valid, the optimum value needs to be calculated using numerical data.

The rest of the paper is organized as follows. In Section II, the system model is introduced and the definitions of the ER and the SSOP are presented. In Section III, the closed-form expression of the upper bound is derived and from this the impact of the radius of the UCA is analyzed. In Section IV, the optimization problem is established and analyzed with respect to the UCA array parameters; an algorithm is then created with the aim of decreasing the SSOP. In Section V, simulation and numerical results are given. Section VI concludes the paper.

II. EXPOSURE REGION AND SPATIAL SECRECY OUTAGE PROBABILITY

A. System Model

As the paper builds on [19], the system model is the same except for the UCA aspect. For this reason, the essential symbols, concepts and derivations for the UCA are described briefly to avoid repetition. Let's assume that Alice is equipped with an antenna array while Bob and Eves have a single antenna. As shown in Fig. 1, Alice is located at the origin point. For convenience, assume that the first element of the UCA is on the positive x-axis. The coordinate is denoted by $z = (d, \theta)$, and subscripts B and E_i are used to represent Bob and the i^{th} Eve respectively, $\forall i \in \mathbb{N}^+$. A general user's location is referred to by z when no subscript is specified. Eves are assumed to be non-colluding and distributed by a homogeneous PPP, Φ_e with density λ_e [27].

On the transmitter side, the UCA has N elements and radius R , and the array vector of UCA is $\mathbf{s}(\theta) = [e^{-j\phi_1(\theta)}, \dots, e^{-j\phi_i(\theta)}, \dots, e^{-j\phi_N(\theta)}]^T$, $\theta \in [0, 2\pi]$, where $\phi_i(\theta) = kR \cos(\theta - \psi_i)$, and $\psi_i = 2\pi(i-1)/N$ is the angular location of the i^{th} element [28] and $k = 2\pi/\lambda$, where λ is the wavelength of the carrier signal. P_t is the transmit power. Given Bob's location information, θ_B , the beamforming weight vector can be set as $\mathbf{w} = \mathbf{s}(\theta_B)/\sqrt{N}$.

Assume a Rician channel with factor K . The channel gain vector is given by

$$\mathbf{h}(z) = d^{-\beta/2} \left(\sqrt{\frac{K}{K+1}} \mathbf{s}(\theta) + \sqrt{\frac{1}{K+1}} \mathbf{g} \right), \quad (1)$$

where $d^{-\beta/2}$ denotes the large-scale path loss with the path loss exponent β of typical values between 2 and 6. The line-of-sight (LOS) component is $\sqrt{\frac{K}{K+1}} \mathbf{s}(\theta)$; the non-LOS component is $\sqrt{\frac{1}{K+1}} \mathbf{g}$, where $\mathbf{g} = [g_1, \dots, g_i, \dots, g_N]^T$, $g_i \sim \mathcal{CN}(0, 1)$, and the elements of \mathbf{g} are independent. Thus, the received signal at z is the sum of the beamforming

178 weighted signals and noise, which can be expressed by $r(z) =$
 179 $\sqrt{P_t} \mathbf{h}^T(z) \mathbf{w}^* x + n_W$, where x is the modulated symbol with
 180 unit power and n_W is the additive white Gaussian noise with
 181 zero mean and variance σ_n^2 .

182 For the ease of subsequent mathematical derivations, let \tilde{h}
 183 be an equivalent channel factor, i.e.,

$$184 \quad \tilde{h} = \mathbf{h}^T(z) \mathbf{w}^* = \sqrt{\frac{K}{K+1}} G(\theta, \theta_B) + \sqrt{\frac{1}{K+1}} g, \quad (2)$$

185 where $G(\theta, \theta_B) = \mathbf{s}(\theta) \mathbf{s}^*(\theta_B) / \sqrt{N}$ is an array factor for any
 186 array type and $g \sim \mathcal{CN}(0, 1)$. According to (2), $|\tilde{h}|^2$ can be
 187 decomposed as follows:

$$188 \quad |\tilde{h}|^2 = \frac{K G^2(\theta, \theta_B)}{K+1} + \frac{g_{Re}^2 + g_{Im}^2}{K+1} + \frac{2\sqrt{K} G(\theta, \theta_B)}{K+1} g_{Re}, \quad (3)$$

189 where g_{Re} and g_{Im} are the real and imaginary part of g ,
 190 so, $g_{Re}, g_{Im} \sim \mathcal{N}(0, \frac{1}{2})$. For the UCA, the array factor was
 191 derived in [28] and is given by

$$192 \quad G(\theta, \theta_B) = \frac{1}{\sqrt{N}} \sum_{i=1}^N e^{jkR[\cos(\theta_B - \psi_i) - \cos(\theta - \psi_i)]}. \quad (4)$$

193 The channel capacity, denoted by $C(z)$, is given by

$$194 \quad C(z) = \log_2 \left(1 + \frac{P_t |\tilde{h}|^2}{\sigma_n^2 d^\beta} \right). \quad (5)$$

195 For convenience, let $C_B = C(z_B)$ and $C_{Ei} = C(z_{Ei})$ denote
 196 the channel capacities of Bob and the i^{th} Eve hereinafter. Due
 197 to the fact that $|\tilde{h}|^2$ scales with $G(\theta, \theta_B)$, a proper design of
 198 $G(\theta, \theta_B)$ can improve C_B while decreasing C_{Ei} .

199 B. Definitions for ER and SSOP for UCA

200 As in [24], let R_B and R_s be the rate of the transmitted code-
 201 words and the rate of the confidential information, respectively.
 202 A secrecy outage event occurs when Eve's channel capacity is
 203 higher than the difference $R_B - R_s$ conditioned on $C_B \geq R_B$,
 204 and the probability of such an event is the SOP. Note that
 205 here two cases are differentiated, i.e., secrecy outage caused
 206 by any Eve conditioned on $C_B \geq R_B$ and data outage given
 207 by $C_B < R_B$. In the latter case, it is typical outage with no
 208 secrecy and thus no secrecy outage. Therefore, the data outage
 209 is not part of the secrecy outage and is beyond the scope of
 210 this paper. In practice, Bob can transmit a one bit feedback to
 211 Alice indicating whether the condition $C_B \geq R_B$ is satisfied.

212 The ER, denoted by Θ , is defined by the geometric region
 213 only where Eves cause the secrecy outage event, i.e., $C_{Ei} >$
 214 $R_B - R_s, \exists z_{Ei} \in \Theta$ conditioned on $C_B \geq R_B$. The boundary
 215 of ER can be derived from $C(z) > R_B - R_s$ and is given
 216 by $D(\theta) = (c_0 P_t |\tilde{h}|^2)^{1/\beta}$, where $c_0 = [\sigma_n^2 (2^{R_B - R_s} - 1)]^{-1}$
 217 is deterministic and is assumed to be constant in this paper.
 218 Thus, $D(\theta)$ is random as $|\tilde{h}|^2$ varies. When the channel is
 219 deterministic, $D(\theta)$ is also deterministic, as shown by the
 220 dashed curve in Fig. 1.

221 Let A denote the size of Θ . For PPP-distributed Eves, the
 222 probability of m Eves being inside $D(\theta)$ can be given by [27]

$$223 \quad \text{Prob}\{m \text{ Eves in } \Theta\} = \frac{(\lambda_e A)^m}{m!} e^{-\lambda_e A}. \quad (6)$$

224 Thus, the SSOP, denoted by p , can be defined by the proba-
 225 bility that any Eve is located inside $D(\theta)$.

$$226 \quad p = 1 - \text{Prob}\{0 \text{ Eve in } \Theta\} = 1 - e^{-\lambda_e A}. \quad (7)$$

227 Note that p is computed by the complementary of the proba-
 228 bility that no Eve is inside Θ . In polar coordinates, (7) can
 229 be derived by

$$230 \quad p = 1 - \exp\left[-\frac{\lambda_e}{2} c_0^{\frac{2}{\beta}} P_t^{\frac{2}{\beta}} \int_0^{2\pi} (|\tilde{h}|^2)^{\frac{2}{\beta}} d\theta\right]. \quad (8)$$

231 The smaller p is, the more secure the transmission to Bob is.
 232 Due to the fact that \tilde{h} is random channel fading, it is more
 233 interesting to study the expectation of p in (8), which reflects
 234 the averaged SSOP \bar{p} ,

$$235 \quad \bar{p} = \mathbb{E}_{|\tilde{h}|} [p]. \quad (9)$$

236 The term \bar{p} in (9) can be expressed by

$$237 \quad \bar{p} = 1 - \int_{-\infty}^{\infty} \int_{-\infty}^{\infty} \exp\left\{-\frac{\lambda_e}{2} c_0^{\frac{2}{\beta}} P_t^{\frac{2}{\beta}} \int_0^{2\pi} \left[\frac{K G^2(\theta, \theta_B)}{K+1}\right.\right. \\ 238 \quad \left.\left. + \frac{x^2 + y^2}{K+1} + \frac{2\sqrt{K} G(\theta, \theta_B)}{K+1} x\right]^{\frac{2}{\beta}} d\theta\right\} \frac{e^{-(x^2+y^2)}}{\pi} dx dy, \quad (10)$$

240 Notice that $G(\theta, \theta_B)$ is a general array factor expression. For
 241 the UCA, p and \bar{p} are obtained by substituting (4) into (8)
 242 and (10).

243 C. An Optimization Problem

244 The focus of this paper is to increase the security level of
 245 the transmission from Alice to Bob, i.e., reducing \bar{p} . To this
 246 end, \bar{p} is first analyzed against the factors in (10). Assume that
 247 the noise variance σ_n^2 , channel factors β and K , the security
 248 related parameters R_B and R_s and the density of Eves λ_e are
 249 fixed. The remaining factors are the transmit power P_t , the
 250 array factor $G(\theta, \theta_B)$ and Bob's location (d_B, θ_B) . Thus, an
 251 optimization problem can be expressed by

$$252 \quad \min \bar{p} \text{ s.t. for all } d_B, \theta_B \quad (11)$$

253 To minimize \bar{p} , the interrelationship between parameters
 254 related to Alice, i.e., P_t and $G(\theta, \theta_B)$, and Bob's location
 255 (d_B, θ_B) should be analyzed. Note that d_B does not appear
 256 in (10) and P_t has a monotonic relationship with \bar{p} . In addition,
 257 the impact of P_t and $G(\theta, \theta_B)$ on \bar{p} are independent according
 258 to (10). In this paper, when studying the impact of $G(\theta, \theta_B)$,
 259 P_t and d_B will be not be included.

260 $G(\theta, \theta_B)$ in (4) depends on the array parameters N and
 261 R as well as Bob's angle θ_B . As the number of antennas N
 262 is normally fixed for a certain UCA, the impact of R will
 263 be mainly discussed against θ_B . Due to the reflection and
 264 rotation symmetry of the UCA, the shape of $G(\theta, \theta_B)$ also has
 265 reflection and rotation symmetry regarding θ_B . An example
 266 of $G(\theta, \theta_B)$ with $\theta_B = 0, \frac{\pi}{4}$ and $N = 8$ is shown in Fig. 2.
 267 As the first element of the UCA lies on the positive x-axis, the
 268 shape of $G(\theta, \theta_B)$ for $\theta_B = \frac{\pi}{4}$ can be obtained by shifting the
 269 shape for $\theta_B = 0$ by $\frac{\pi}{4}$, and vice versa. At the same time,
 270 the two shapes are symmetric regarding to $\theta_B = \frac{\pi}{8}$. In general,

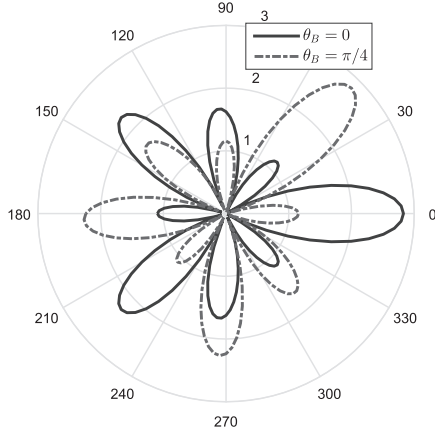


Fig. 2. $G(\theta, \theta_B)$ for $\theta_B = 0$ and $\theta_B = \frac{\pi}{4}$. $N = 8$ and $R = 0.8\lambda$.

271 $G(\theta, \theta_B)$ at $\pm(\theta_B \pm 2\pi/N)$ are of the same shape. Therefore,
 272 it suffices to study $G(\theta, \theta_B)$ only in $\theta_B \in [0, \frac{\pi}{N}]$ instead of
 273 $[0, 2\pi]$.

274 The expression of \bar{p} in (10) is complex and can be calculated
 275 numerically. However, it is not tractable to obtain in closed-
 276 form expression, except for the deterministic channel when
 277 $\beta = 2$. Therefore, an upper bound expression for \bar{p} , denoted
 278 by \bar{p}_{up} , should be derived in closed-form for UCA in order
 279 to facilitate detailed theoretical analysis. Notice that for other
 280 array types, the method of analyzing \bar{p} via closed-form expres-
 281 sion of \bar{p}_{up} still works. If closed-form expressions of \bar{p}_{up} do
 282 not exist, appropriate approximations or numerical results can
 283 be used based on the particular form of given $G(\theta, \theta_B)$.

284 III. CLOSED-FORM EXPRESSION FOR 285 THE UPPER BOUND FOR SSOP

286 A. Derivation of the Upper Bound for UCA

287 Firstly, a general upper bound is briefly introduced as
 288 follows, based on which the particular upper bound for UCA
 289 can be derived. For a given λ_e and K , \bar{p}_{up} can be derived
 290 using Jensen's inequality.

$$291 \bar{p}_{up} = 1 - \exp\left\{-\lambda_e \pi \left[c_0 P_t \frac{K A_0 + 2\pi}{2\pi(K+1)} \right]^{\frac{2}{\beta}} \right\}, \quad (12)$$

292 where A_0 denotes the pattern area and is given by,

$$293 A_0 = \int_0^{2\pi} G^2(\theta, \theta_B) d\theta. \quad (13)$$

294 The derivation is described in [19]. According to (12), \bar{p}_{up} is
 295 monotonically increasing with A_0 for any K and β . Therefore,
 296 \bar{p}_{up} can be analyzed via A_0 .

297 Notice that the expression of A_0 in (13) contains $G(\theta, \theta_B)$
 298 which is a general expression. To obtain the particular expres-
 299 sion for the UCA, the expression of A_0 needs to be determined.
 300 We can isolate θ to solve the integral in (4).

$$301 G^2(\theta, \theta_B) = \frac{1}{N} \sum_{i,j} e^{jkR[\cos(\theta_B - \psi_i) - \cos(\theta_B - \psi_j)]} \\ 302 \cdot e^{-jkR[\cos(\theta - \psi_i) - \cos(\theta - \psi_j)]}, \quad (14)$$

where $\sum_{i,j}$ represents $\sum_{i=1}^N \sum_{j=1}^N$ and $\cos(\theta - \psi_i) -$
 303 $\cos(\theta - \psi_j)$ can be further derived by 304

$$305 \cos(\theta - \psi_i) - \cos(\theta - \psi_j) = 2 \sin\left(\theta - \frac{i+j-2}{N}\pi\right) \sin\left(\frac{i-j}{N}\pi\right). \quad (15)$$

Let $W_{i,j} = 2 \sin(\frac{i-j}{N}\pi)$ and $Z_{i,j} = \frac{i+j-2}{N}\pi$. Substituting (15)
 307 into (14), $G^2(\theta, \theta_B)$ can be derived as 308

$$309 \frac{1}{N} \sum_{i,j} e^{jkRW_{i,j} \sin(\theta_B - Z_{i,j})} \cdot e^{-jkRW_{i,j} \sin(\theta - Z_{i,j})}. \quad (16)$$

According to $J_n(x) = \frac{1}{2\pi} \int_{-\pi}^{\pi} e^{j(n\tau - x \sin \tau)} d\tau$, where $J_n(x)$ is
 310 the Bessel function of the first kind with order n , the following
 311 integration can be derived. 312

$$\int_0^{2\pi} e^{-jkRW_{i,j} \sin(\theta - Z_{i,j})} d\theta \\ 313 = \int_{-Z_{i,j}}^{2\pi - Z_{i,j}} e^{j[0\cdot\tau - kRW_{i,j} \sin \tau]} d(\tau + Z_{i,j}) \\ 314 = \int_{-\pi}^{\pi} e^{j[0\cdot\theta - kRW_{i,j} \sin \tau]} d\tau = 2\pi J_0(kRW_{i,j}) \quad (17) \quad 315$$

Note that in the second step, the upper and lower limits can be
 316 transformed to π and $-\pi$, because $\sin \tau$ is a periodic function
 317 with a period of 2π . 318

Combining (16) and (17), A_0 in (13) can be written as 319

$$320 A_0 = \frac{2\pi}{N} \sum_{i,j} J_0(kRW_{i,j}) e^{jkRW_{i,j} \sin(\theta_B - Z_{i,j})}. \quad (18)$$

The double summation of Bessel functions in (18) is
 321 intractable to analyze. In the following, A_0 will be further
 322 simplified. Let $A_{0,i,j}$ denote each summation term in (18), 323

$$324 A_{0,i,j} = \frac{2\pi}{N} J_0(kRW_{i,j}) e^{jkRW_{i,j} \sin(\theta_B - Z_{i,j})}. \quad (19)$$

It is deduced that $W_{i,j} = -W_{j,i}$ and $Z_{i,j} = Z_{j,i}$. Considering
 325 that $J_n(-x) = (-1)^n J_n(x)$ and $J_0(x)$ is a real number, it can
 326 be deduced that $A_{0,i,j} = A_{0,j,i}^*$. In addition, it can be shown
 327 from the expression of $W_{i,j}$ and $Z_{i,j}$ that $W_{i,j+N} = -W_{i,j}$.
 328 Similarly, $\sin(\theta_B - Z_{i,j+N}) = -\sin(\theta_B - Z_{i,j})$. Thus, it can
 329 be determined found that $A_{0,i,j} = A_{0,i,j+N}$. 330

A table of $A_{0,i,j}$ is shown in Fig.3 to illustrate how to
 331 use the previous properties to simplify the summation of A_0
 332 in (18). For $N = 4$, the table is extended to $j = 8$. As $A_{0,i,j} =$
 333 $A_{0,i,j+N}$, the blue region is equivalent to the green region.
 334 Instead of adding $A_{i,j}$ for i, j from 1 to N , the summation
 335 can now be executed diagonally. For convenience, let $n = i - j$.
 336 Then, $W_n = W_{i,j} = 2 \sin(\frac{n}{N}\pi)$. The terms $A_{0,i,j}$ on the red
 337 diagonal lines in the table have the same W_n . In the table,
 338 $\frac{N}{\pi} Z_{i,j}$ is allocated according to their indices i and j . Given
 339 $n = i - j$, it can be derived that 340

$$341 Z_{n,i} = Z_{i,j} = \frac{i+j-2}{N}\pi = \frac{2i-n-2}{N}\pi. \quad (20)$$

Thus, it can be derived that 342

$$343 A_{0,n,i} = A_{0,i,j} = \frac{2\pi}{N} J_0(kRW_n) e^{jkRW_n \sin(\theta_B - Z_{n,i})}. \quad (21)$$

| $\frac{N}{\pi} Z_{i,j} = i+j-2$ | | | | | | | | | |
|---------------------------------|---------|---|---|-------|------------------------|---|--------|--------|--------|
| $i \setminus j$ | 1 | 2 | 3 | 4 | 5 | 6 | 7 | 8 | |
| 1 | 0 | 1 | 2 | 3 | extened table: $j > 4$ | | | | |
| 2 | 1 | 2 | 3 | 4 | 5 | | | | |
| 3 | 2 | 3 | 4 | 5 | 6 | 7 | | | |
| 4 | 3 | 4 | 5 | 6 | 7 | 8 | 9 | | |
| | $n=i-j$ | | | $n=0$ | | | $n=-1$ | $n=-2$ | $n=-3$ |

 Fig. 3. Table for $Z_{i,j}$, $N = 4$.

A_0 is the summation of all elements in the original table (i.e., $i, j = 1, \dots, 4$). Because $A_{0,i,j+N} = A_{0,i,j}$, the calculation of A_0 can be executed by replacing the lower triangle in the original table (i.e., $i > j$) with the lower triangle in the extended table (i.e., $i > j - N$). In the new formation of A_0 , which is a parallelogram table, the summation can be carried out along the diagonal lines from $n = 0$ to $n = -(N - 1)$. For any n , the summation of $A_{0,n,i}$ includes N terms with $Z_{n,i}$. Thus, (18) can be converted into

$$\begin{aligned}
 A_0 &= \sum_{i=1}^N \sum_{j=1}^N A_{0,i,j} = \sum_{n=0}^{-(N-1)} \sum_{i=1}^N A_{0,n,i} \\
 &= \sum_{n=0}^{-(N-1)} \sum_{i=1}^N \frac{2\pi}{N} J_0(kRW_n) e^{jkRW_n \sin(\theta_B - Z_{n,i})} \\
 &= \frac{2\pi}{N} \sum_{n=0}^{-(N-1)} J_0(kRW_n) \sum_{i=1}^N e^{jkRW_n \sin(\theta_B - Z_{n,i})}. \quad (22)
 \end{aligned}$$

According to Jacobi-Anger expansion $e^{ja \sin \gamma} = \sum_{m=-\infty}^{\infty} J_m(a) e^{jm\gamma}$, (22) can be further derived by (23) at the bottom of the following page.

When $m = lN$, $l \in \mathbb{Z}$, $e^{j\pi \frac{m}{N}(n+2)} = e^{jl n \pi} e^{j2\pi l} = e^{jl n \pi}$ and

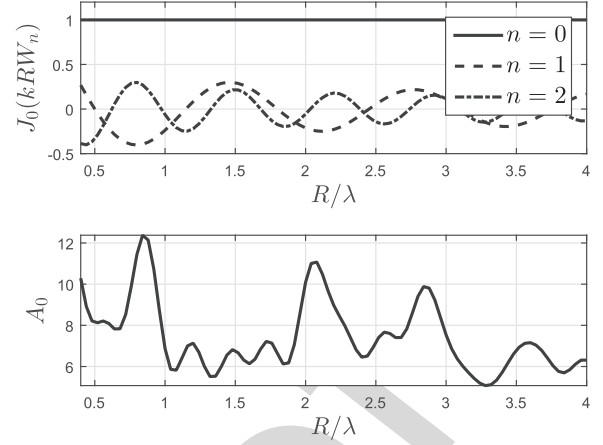
$$\sum_{i=1}^N e^{-j2\pi \frac{m}{N} i} = \sum_{i=1}^N e^{-j2\pi l i} = N. \quad (24)$$

When $m \neq lN$,

$$\sum_{i=1}^N e^{-j2\pi \frac{m}{N} i} = e^{-j2\pi \frac{m}{N}} \frac{1 - e^{-j2\pi \frac{m}{N} N}}{1 - e^{-j2\pi \frac{m}{N}}} = 0. \quad (25)$$

Thus, it can be derived that

$$\begin{aligned}
 A_0 &= \frac{2\pi}{N} \sum_{n=0}^{-(N-1)} J_0(kRW_n) \sum_{l=-\infty}^{\infty} J_{lN}(kRW_n) e^{jlN\theta_B} e^{jl n \pi} \\
 &= 2\pi \sum_{n=0}^{-(N-1)} J_0(kRW_n) \sum_{l=-\infty}^{\infty} J_{lN}(kRW_n) e^{jlN\theta_B} (-1)^{ln} \\
 &= 2\pi \sum_{n=0}^{N-1} J_0(-kRW_n) \sum_{l=-\infty}^{\infty} (-1)^{-ln} J_{lN}(-kRW_n) e^{jlN\theta_B} \\
 &= 2\pi \sum_{n=0}^{N-1} J_0(kRW_n) \sum_{l=-\infty}^{\infty} (-1)^{ln+lN} J_{lN}(kRW_n) e^{jlN\theta_B}. \quad (26)
 \end{aligned}$$


 Fig. 4. Upper plot: Examples of $J_0(kRW_n)$ versus R . Lower plot: A_0 versus R . $N = 8$, $\theta_B = 0^\circ$.

Substituting (26) in (13), the closed-form expression for \bar{p}_{up} in (12) can be obtained. Compared to (13), the expression of A_0 in (26) consists of a finite summation of $J_0(\cdot)$ and an infinite summation of $J_{lN}(\cdot)$, which can provide asymptotic analysis.

B. Impact of R on A_0

As discussed in Section II-C, the impact of R will be used as a starting point to formulate the optimization problem. In the low region of x , the Bessel function $J_{lN}(x)$ in (26) is negligible for high order lN , i.e., $lN \gg 1$. Let x_0 denote the upper limit of the range $x \in [0, x_0]$ where $J_{lN}(x)$ is negligible for certain lN . Then, the specific value x_0 depends on the order lN . As the order lN increases, x_0 increases and eventually exceeds the value of $2kR$, which is the upper limit of $x = kRW_n$ in (26) for a fixed R . Once x_0 becomes larger than $2kR$, all $J_{lN}(x)$ for $l \geq 1$ are negligible in the range $(0, 2kR]$. Thus, for sufficiently large N , A_0 in (26) can be approximated by

$$A_0 \approx 2\pi \sum_{n=0}^{N-1} J_0^2(kRW_n). \quad (27)$$

The asymptotic behavior of A_0 versus R can be analyzed through (27). As shown in the upper plot in Fig.4, when $n = 0$, $J_0(kRW_0) = 1$, because $W_0 = 0$ and $J_0(0)$ is a constant that is irrelevant to R . When $n \neq 0$, $J_0(kRW_n)$ gradually decreases with some fluctuation as R increases, which is determined by the nature of $J_0(\cdot)$. Notice that in the asymptotic expression in (27), the angle θ_B is neglected. When N is not large enough, the term $J_{lN}(kRW_n) e^{jlN\theta_B}$ also needs to be considered. As $J_n(x)$ decreases and approaches zero with different convergence speed, the summation of a series of Bessel functions, i.e., A_0 , in general decreases and approaches a certain value as R increases. Due to the difference in the converging speed of $J_{lN}(kRW_n)$, there are some fluctuations.

An example of A_0 versus R is shown in the lower plot in Fig.4 where $N = 8$ and $\theta_B = 0^\circ$. It can be seen that A_0 fluctuates as R increases, because the curve is a superposition of $J_{lN}(kRW_n)$ with different orders lN . Thus,

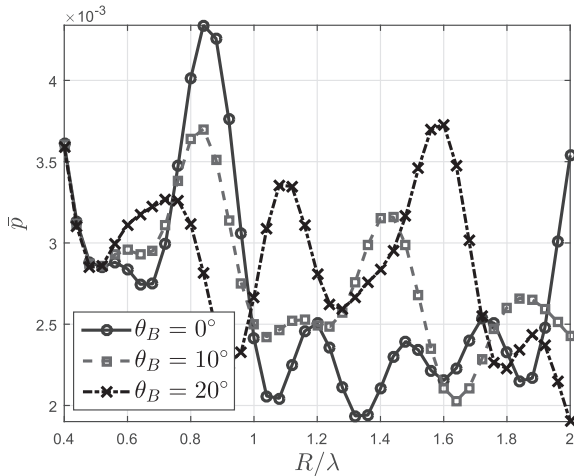


Fig. 5. \bar{p} versus R for different values of θ_B , $N = 8$, $P_t/\sigma_n^2 = 15$ dB, $R_B = 3.4594$ bps/Hz, $R_s = 1$ bps/Hz, $\lambda_e = 1 \times 10^{-4}$.

in a local region, e.g., $R < 2\lambda$, the minimum value does not necessarily correspond to a large or small R , which leads to the optimization problem for R .

IV. OPTIMIZATION ALGORITHM

A. Refined Optimization Problem

As mentioned in Section III-B, R can be properly designed according to θ_B to achieve a local minimum value in a certain range of R . According to Section II-C, d_B is not involved in the expression of \bar{p} . Thus, the optimization problem can be solved by optimizing R according to θ_B .

It is worth noticing that although the closed-form expression of \bar{p}_{up} provides an asymptotic analysis on the impact of R , it does not provide accurate results for the optimum value for R . As it is intractable to analyze the expression of \bar{p} in (10), we will use numerical results to determine this.

Examples of \bar{p} versus R for different θ_B are shown in Fig. 5 where $N = 8$. For simplicity, let $K \rightarrow \infty$ and $\beta = 2$, i.e., the channel is degraded to a free-space channel. More results for Rician fading channel will be provided in Section V-A. For the purpose of MATLAB simulation, the value of R is taken by a step of 1 cm in the range $[0.4\lambda, 2\lambda]$. Typical values of θ_B , i.e., $\theta_B = 0^\circ, 10^\circ, 20^\circ$, are taken for the UCA with $N = 8$. Fig. 5 depicts the fluctuating behavior of \bar{p} with respect to R for different values of θ_B . It can be seen that the curves for different θ_B vary. Therefore, for each θ_B , the local minimum of \bar{p} in the range $R \in [0.4\lambda, 2\lambda]$ is given by a different value of R . This suggests that by varying θ_B , a different R should be chosen in order to achieve a minimum \bar{p} . However, this is

not practical because R is usually predefined for an existing UCA.

Since R can only be a particular value, the optimum value R_{opt} needs to be pre-designed. To this end, the minimum mean error is used to find R_{opt} in a certain range of R that produces the minimum \bar{p} for all possible $\theta_B \sim \mathcal{U}(0, 2\pi)$. To establish the cost function, imagine that R is adjustable, which provides the hypothetical function of \bar{p}_{min} with respect to θ_B . Notice that the value of \bar{p}_{min} for each θ_B is, in fact, given by a different value of R . To find R_{opt} , let the mean error, denoted by $err(R)$, be the mean value of the difference between \bar{p} and \bar{p}_{min} over the range $\theta_B \in [0, 2\pi]$,

$$err(R) = \mathbb{E}_{\theta_B}[\bar{p} - \bar{p}_{min}]. \quad (28)$$

Note that the mean error is used instead of the mean square error because $\bar{p} - \bar{p}_{min}$ is always non-negative. Thus, R_{opt} can be found by

$$R_{opt} = \arg \min_R err(R). \quad (29)$$

(29) can be converted into the following expression, the derivation of which is in Appendix A.

$$R_{opt} = \arg \min_R \bar{\bar{p}}, \quad (30)$$

where $\bar{\bar{p}}$ is the averaged \bar{p} over Bob's angles and is defined by

$$\bar{\bar{p}} = \frac{1}{2\pi} \int_0^{2\pi} \bar{p} d\theta_B. \quad (31)$$

B. Analysis and Implementation of Optimization Algorithm

Substituting the expression of \bar{p} in (10) into (31), the expression of $\bar{\bar{p}}$ can be obtained,

$$\begin{aligned} \bar{\bar{p}} = & 1 - \frac{1}{2\pi} \int_{-\infty}^{\infty} \int_{-\infty}^{\infty} \int_0^{2\pi} \exp\left\{-\frac{\lambda_e}{2}(c_0 P_t)^{\frac{2}{\beta}}\right. \\ & \times \int_0^{2\pi} \left[\frac{K G_C^2(\theta, \theta_B)}{K+1} + \frac{x^2 + y^2}{K+1}\right. \\ & \left. \left. + \frac{2\sqrt{K} G_C(\theta, \theta_B)}{K+1} x\right]^{\frac{2}{\beta}} d\theta\right\} \frac{e^{-(x^2+y^2)}}{\pi} d\theta_B dx dy. \end{aligned} \quad (32)$$

Although (32) can be numerically calculated, it is intractable to analyze. Thus, the upper bound, denoted by $\bar{\bar{p}}_{up}$, is required for theoretical analysis.

Theorem 1:

$$\bar{\bar{p}}_{up} = 1 - \exp\left\{-\lambda_e \pi \left[\frac{c_0 K \bar{A}_0}{2\pi(K+1)} + \frac{c_0}{K+1}\right]^{\frac{2}{\beta}}\right\}, \quad (33)$$

where \bar{A}_0 is the expectation of A_0 over θ_B and is given by

$$\bar{A}_0 = \frac{1}{2\pi} \int_0^{2\pi} A_0 d\theta_B = 2\pi \sum_{n=0}^{N-1} J_0^2(kRW_n). \quad (34)$$

$$\begin{aligned} A_0 &= \frac{2\pi}{N} \sum_{n=0}^{-(N-1)} J_0(kRW_n) \sum_{i=1}^N \sum_{m=-\infty}^{\infty} J_m(kRW_n) e^{jm(\theta_B - Z_{n,i})} = \frac{2\pi}{N} \sum_{n=0}^{-(N-1)} J_0(kRW_n) \sum_{m=-\infty}^{\infty} J_m(kRW_n) e^{jm\theta_B} \sum_{i=1}^N e^{-jmZ_{n,i}} \\ &= \frac{2\pi}{N} \sum_{n=0}^{-(N-1)} J_0(kRW_n) \sum_{m=-\infty}^{\infty} J_m(kRW_n) e^{jm\theta_B} e^{j\pi \frac{m}{N}(n+2)} \sum_{i=1}^N e^{-j2\pi \frac{m}{N}i}. \end{aligned} \quad (23)$$

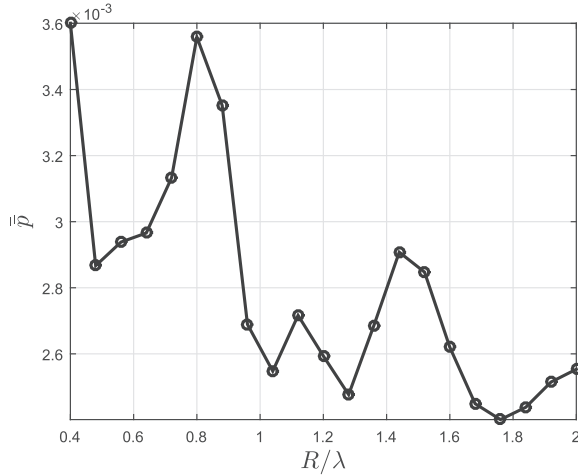


Fig. 6. \bar{p} versus R for all θ_B , $N = 8$, $P_t/\sigma_n^2 = 15$ dB, $R_B = 3.4594$ bps/Hz, $R_S = 1$ bps/Hz, $\lambda_e = 1 \times 10^{-4}$.

469 The proof of Theorem 1 is given in Appendix B. It can be seen
 470 that (34) has a similar composition to A_0 in (26). Therefore,
 471 \bar{A}_0 in general decreases with some fluctuations as R increases.
 472 Due to the monotonically increasing relationship between \bar{p}_{up}
 473 and \bar{A}_0 , it can be deduced that \bar{p} decreases in general with
 474 some fluctuations as R increases.

475 Because \bar{p} fluctuates in a certain range of R , there must
 476 exist at least one local minimum. Numerical results are used
 477 to find R_{opt} in (30). For example, choosing $N = 8$ and
 478 $R \in [0.4\lambda, 2\lambda]$, the results of \bar{p} shown in Fig. 6 are obtained
 479 where the channel is chosen as a free-space channel. It can
 480 be seen that there is more than one local minimum. In the
 481 range $R \in [0.4\lambda, 2\lambda]$, $R_{opt} = 1.76\lambda$ gives the minimum \bar{p}
 482 as 2.4×10^{-3} . Compared to the maximum value of \bar{p} that is
 483 3.6×10^{-3} in the same range, there is a 33% reduction in
 484 the value of \bar{p} . This indicates that by choosing an appropriate
 485 value of R , the averaged SSOP can be dramatically reduced.

486 The numerical implementation of the algorithm is shown in
 487 Algorithm 1. The continuous ranges of R , θ_B , θ are discretized
 488 with steps of ΔR , $\Delta\theta_B$ and $\Delta\theta$, respectively. In addition,
 489 a limit value Q is used when calculating integral from $-\infty$
 490 to ∞ in (32). For a normal distribution, a realistic value is set
 491 for Q , namely 3. Let N_R , N_{θ_B} , N_{θ} and N_Q be the number of
 492 samples for R , θ_B , θ and the integration range Q respectively,
 493 which determines the iteration numbers.

494 There are two main steps in the optimization algorithm.
 495 The first step is from line 3 to 15, where \bar{p} for a range of
 496 discretized R is calculated. Notice that the integrals in (32)
 497 are implemented via iterated summation from line 6 to 15. The
 498 second step section is from line 16 to 21, where the minimum
 499 value \bar{p}_{min} in the vector \bar{p} is searched to find R_{opt} which is
 500 the output of the optimization algorithm.

501 The accuracy of the result increases with number of sam-
 502 ples; however, the computational complexity also increases.
 503 The running time of the numerical implementation is approxi-
 504 mately $O(N_R N_{\theta_B} N_Q^2 N_{\theta})$. There is no specific restriction on the
 505 sampling interval as long as the chosen resolution generates a
 506 reasonable value.

Algorithm 1 Optimization of R for Fixed N .

INPUT: σ_n^2 , β , K , R_B , R_S , λ_e , λ , P_t , N

INPUT: R_1 , R_2 , ΔR ; θ_{B1} , θ_{B2} , $\Delta\theta_B$; θ_1 , θ_2 , $\Delta\theta$; Q , ΔQ

OUTPUT: R_{opt}

```

1: discretize  $R$ ,  $\theta_B$ ,  $\theta$ ,  $Q$ 
2: calculate  $N_R$ ,  $N_{\theta_B}$ ,  $N_{\theta}$ ,  $N_Q$  and  $c_0$ 
3: create an  $1 \times N_R$  empty vector of  $\bar{p}$  with index  $idx$ 
4: for each value of  $R \in [R_1, R_2]$ ,  $\theta_B \in [\theta_{B1}, \theta_{B2}]$  do
5:    $S_1 = 0$ 
6:   for each value of  $x, y \in [-Q, Q]$  do
7:      $S_2 = 0$ 
8:     for each value of  $\theta \in [\theta_1, \theta_2]$  do
9:        $S_2 = S_2 +$ 
10:         $\left[ \frac{KG^2(\theta, \theta_B) + x^2 + y^2 + 2\sqrt{K}G(\theta, \theta_B)x}{K+1} \right]^{\frac{2}{\beta}} \Delta\theta$ 
11:     end for
12:      $S_1 = S_1 + \exp\{-\frac{\lambda_e}{2}(P_t c_0)^{\frac{2}{\beta}} S_2\} \frac{e^{-(x^2+y^2)}}{\pi} \Delta Q^2$ 
13:   end for
14:    $\bar{p}(idx) = \bar{p}(idx) + (1 - S_1)/N_{\theta_B}$ 
15: end for
16: initialization:  $R_{opt} = R_1$ ,  $\bar{p}_{min} = \bar{p}(1)$ 
17: for each value of  $R \in [R_1, R_2]$  do
18:   if  $\bar{p}_{min} > \bar{p}(idx)$  then
19:     reassignment:  $R_{opt} = R$ ,  $\bar{p}_{min} = \bar{p}(idx)$ 
20:   end if
21: end for

```

V. SIMULATION AND NUMERICAL RESULTS

507 In this section, we first provide simulation results for \bar{p}
 508 in (10) and then numerical results for \bar{p} in (32) over the Rician
 509 channel with a wider range of values of K and β . Next, the
 510 numerical results of the upper bounds \bar{p}_{up} and \bar{p}_{up} are shown
 511 in comparison with \bar{p} and \bar{p} to demonstrate the validity of the
 512 upper bounds. In the end, we investigate a common problem
 513 in antenna array, i.e., the mutual coupling and its effect on \bar{p} .
 514

A. More Results for Rician Fading Channels

515 In Section IV-B, numerical results are used to show the
 516 properties of \bar{p} versus R . Firstly, the simulation results are
 517 provided to validate the expressions of \bar{p} in (10) that is derived
 518 from the expression in (9) which contains Gaussian random
 519 variables via $|\tilde{h}^2|$ according to (3). We choose $K = 10$ and
 520 $\beta = 3$ as an example to compare the numerical results based
 521 on the expression in (10) and the simulation results based
 522 on the expression in (9). We ran Monte Carlo simulations to
 523 generate 1×10^4 samples of g_{Re} and g_{Im} in (3). As stated in
 524 Section II-C, the noise variance σ_n^2 , channel factors β and K ,
 525 the security related parameters R_B and R_S and the density
 526 of Eves λ_e are assumed to be constant; the transmit power
 527 P_t does not affect the impact of the array parameters to the
 528 SSOP. In this section, P_t and σ_n^2 are set to -65 dBm and
 529 -80 dBm, respectively. The rate of the transmitted codewords
 530 R_B is set to 3.4594 bps/Hz which corresponds to a received
 531 SNR of 10 dB for Bob. The rate of the confidential information
 532 R_S is set to be smaller than R_B , e.g., 1 bps/Hz as used in [18].
 533 The density of Eves is set to 1×10^{-4} which means 100 Eves
 534

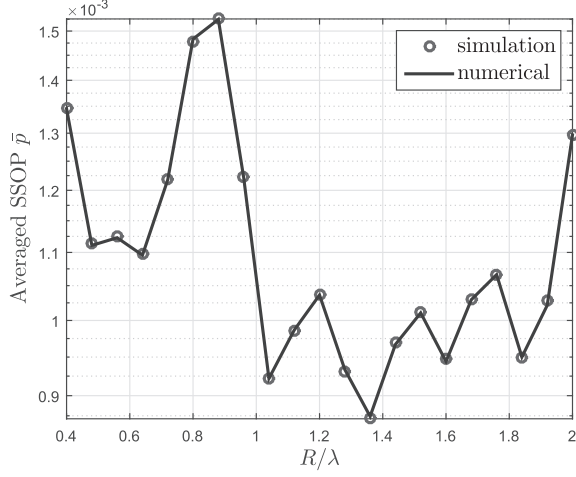


Fig. 7. Simulation and numerical results for \bar{p} versus R ; $K = 10$, $\beta = 3$, $\theta_B = 0^\circ$, $P_t/\sigma_n^2 = 15$ dB, $R_B = 3.4594$ bps/Hz, $R_s = 1$ bps/Hz, $\lambda_e = 1 \times 10^{-4}$.

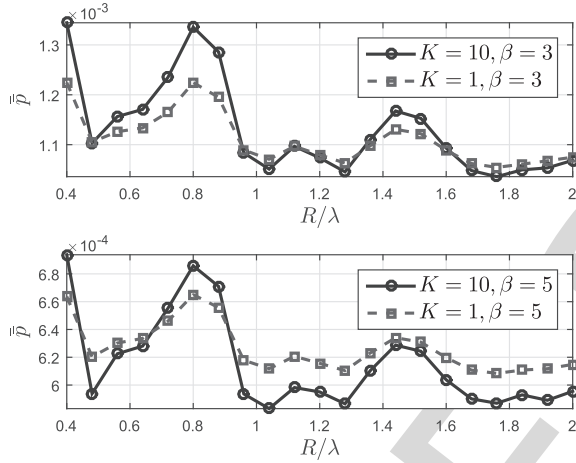


Fig. 8. Numerical results for \bar{p} versus R ; $P_t/\sigma_n^2 = 15$ dB, $R_B = 3.4594$ bps/Hz, $R_s = 1$ bps/Hz, $\lambda_e = 1 \times 10^{-4}$.

in 1000×1000 m². Finally, the radius of the UCA is set to $[0.4\lambda, 2\lambda]$, which corresponds to $[5, 25]$ cm for 2.4 GHz frequency. For comparison, a commercial uniform circular array FCI-3710 developed by Fidelity Comtech has 15.24 cm radius [29]. The simulation and numerical results plotted in Fig. 7 show a good match between them, which verifies the validity of the expressions in (10).

Secondly, a wider range of K and β for Rician channel will be examined. We choose typical value of $\beta = 3, 5$ and $K = 1, 10$. The results of \bar{p} is calculated according to (32). As shown in Fig. 8, all curves exhibit similar trend with regard to R to the curve in Fig. 6 where $K \rightarrow \infty$ and $\beta = 2$. In addition, for both curves in Fig. 8, the optimum value R_{opt} in the range $R \in [0.4\lambda, 2\lambda]$ is 1.76λ . It means that the optimum value of R in a certain range is valid for Rician channels with different K and β .

B. Numerical Results of the Upper Bounds

Next, closed-form expressions of \bar{p}_{up} and \bar{p}_{up} are derived in Section III-A and Section IV-B, respectively, in order to facilitate analysis. Here, some numerical results are shown to

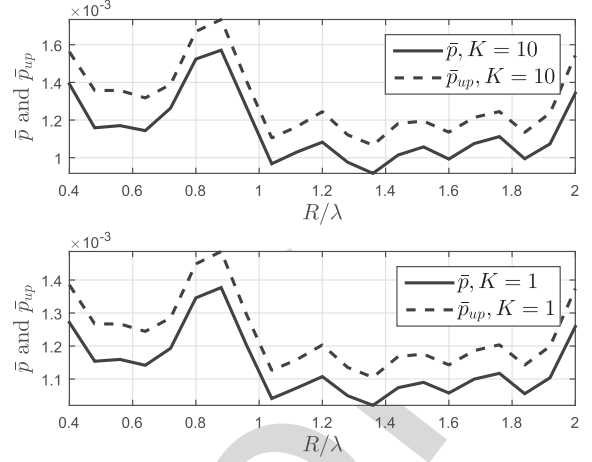


Fig. 9. Numerical results for \bar{p} and \bar{p}_{up} versus R ; $\beta = 3$, $P_t/\sigma_n^2 = 15$ dB, $R_B = 3.4594$ bps/Hz, $R_s = 1$ bps/Hz, $\lambda_e = 1 \times 10^{-4}$.

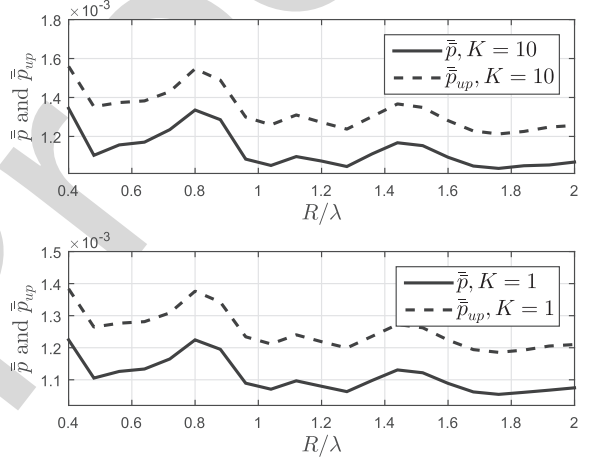


Fig. 10. Numerical results for \bar{p} and \bar{p}_{up} versus R ; $\beta = 3$, $P_t/\sigma_n^2 = 15$ dB, $R_B = 3.4594$ bps/Hz, $R_s = 1$ bps/Hz, $\lambda_e = 1 \times 10^{-4}$.

demonstrate that the upper bounds can reflect the fluctuating behavior of \bar{p} and \bar{p} against R .

In Fig. 9, the results for \bar{p} and \bar{p}_{up} versus R are shown for typical values of $\beta = 3$ and $K = 1, 10$. It can be seen that the curves of \bar{p}_{up} have a similar shape to the curves of \bar{p} , and the value of \bar{p}_{up} is close to \bar{p}_{up} . This suggests that the upper bound can very well reflect the property of \bar{p} .

In Fig. 10, the results for \bar{p} and \bar{p}_{up} versus R are shown for typical values of $\beta = 3$ and $K = 1, 10$. It can be seen that the curves for \bar{p} and \bar{p}_{up} have a similar shape, and the values of \bar{p} and \bar{p}_{up} are close to each other, which means that \bar{p}_{up} is a good upper bound.

C. Impact of Mutual Coupling

The mutual coupling is caused by energy absorption between proximate antennas and causes distortion to the array factor $G(\theta, \theta_B)$, and thus affects \bar{p} and the optimization algorithm. In this paper, we choose the NEC tool [26] to build a numerical model as an example to examine the impact of the mutual coupling, although any analytical model will apply.

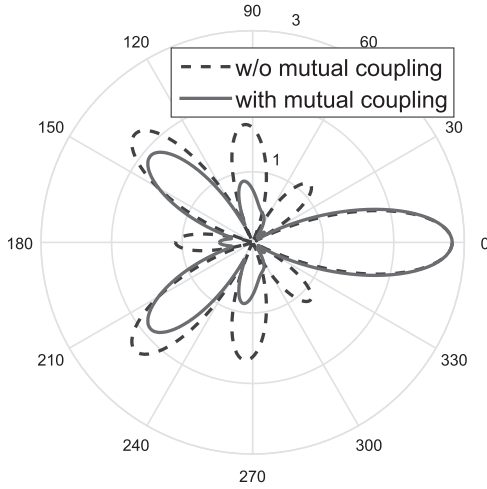


Fig. 11. Example of theoretical and NEC simulated patterns, $N = 8$, $R = 0.8\lambda$, $\theta_B = 0^\circ$.

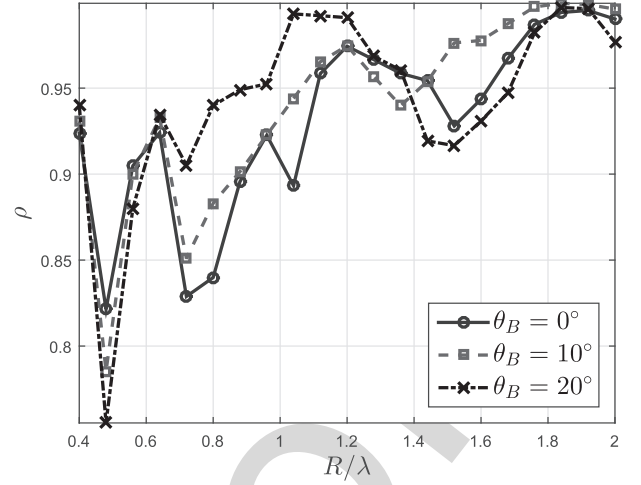


Fig. 12. Correlation coefficients between theoretical and NEC simulated patterns, $N = 8$, $P_t/\sigma_n^2 = 15$ dB, $R_B = 3.4594$ bps/Hz, $R_s = 1$ bps/Hz, $\lambda_e = 1 \times 10^{-4}$.

574 The NEC tool serves as a numerical method to calculate array patterns that include the mutual coupling effect, and its results are well accepted in the literature [30], [31].

575 An example shown in Fig. 11 illustrates the difference caused by the mutual coupling for system configurations with $N = 8$, $R = 0.8\lambda$, $\theta_B = 0^\circ$. The array pattern with the mutual coupling is calculated by the NEC simulation. It can be seen that there is not much difference in the main beam, but with deviation in the sidelobes.

576 To measure the array pattern distortion caused by the mutual coupling, Pearson's correlation coefficient, denoted by ρ , is adopted. It measures the correlation between two variables X and Y , as defined by

$$\rho = \frac{\text{cov}(X, Y)}{\text{std}(X) \cdot \text{std}(Y)}, \quad (35)$$

577 where $\text{cov}(\cdot, \cdot)$ stands for the covariance and $\text{std}(\cdot)$ the standard deviation. ρ between the theoretical array pattern and the simulated array pattern via NEC tool can be calculated to quantify their similarity. The larger ρ is, the more alike two patterns are.

578 The patterns of the UCA with a range of radius are simulated in NEC. For $N = 8$, typical values are chosen, i.e., $\theta_B = 0^\circ, 10^\circ, 20^\circ$ in the range $R = [0.4\lambda, 2\lambda]$. The correlation coefficient, ρ , between the theoretical and NEC patterns is calculated and the results are shown in Fig. 12. It can be seen that ρ is generally above 0.8 in the range of $R = [0.4\lambda, 2\lambda]$, except for $R = 0.48\lambda$. This shows that the mutual coupling does not cause a significant distortion to the pattern of UCA. The high correlation between the theoretical and NEC patterns indicates that the optimization algorithm, which is based on empirical results on the theoretical patterns, can still work when considering the mutual coupling.

579 On the other hand, there exists some differences between the theoretical and NEC patterns, which means that when calculating R_{opt} in the numerical implementation of the optimization algorithm, the NEC simulation data instead of the theoretical data should be used. To compare with Fig. 5, the same array parameters are adopted, i.e., $N = 8$ and $R \in [0.4\lambda, 2\lambda]$,

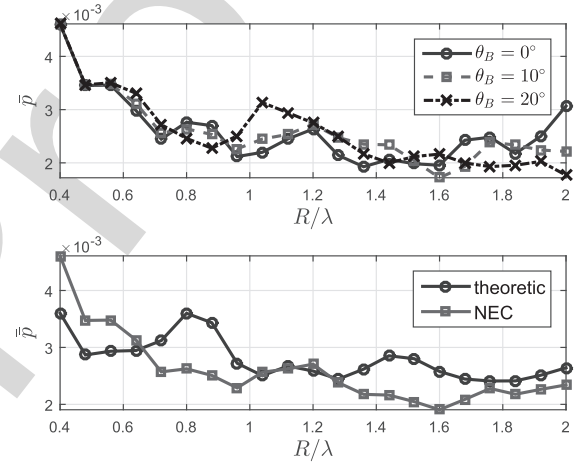


Fig. 13. Upper plot: $\bar{\rho}$ versus R . Lower plot: $\bar{\bar{\rho}}$ versus R . $N = 8$, $P_t/\sigma_n^2 = 15$ dB, $R_B = 3.4594$ bps/Hz, $R_s = 1$ bps/Hz, $\lambda_e = 1 \times 10^{-4}$.

and $\bar{\rho}$ with the mutual coupling is calculated based on the NEC simulation data. The results are shown in the upper plot in Fig. 13. Compared to Fig. 5, it is not hard to notice the similarity between the theoretical and NEC simulated curves for the same θ_B , which can be explained by the high correlation between them, as shown in Fig. 12.

Because of the differences between the theoretical and NEC simulated results, $\bar{\bar{\rho}}$ in Fig. 6 needs to be re-calculated based on the NEC simulation data, in order to find R_{opt} . The lower plot in Fig. 13 shows $\bar{\bar{\rho}}$ based on the NEC simulation data in comparison with the theoretical curve. It can be seen that the optimum value for the NEC simulation data is $R_{opt} = 1.6\lambda$ compared to $R_{opt} = 1.76\lambda$ for the theoretical result. By choosing $R_{opt} = 1.6\lambda$, the value of $\bar{\bar{\rho}}$ is reduced dramatically by about 59% compared to the maximum value of $\bar{\bar{\rho}}$ at $R = 0.4\lambda$.

VI. CONCLUSIONS

This paper investigated the security performance of ER-based beamforming system with the UCA in the presence of PPP distributed Eves in Rician fading channel. With the aid

of the expression of the averaged SSOP and the closed-form expression of its upper bound, an optimization algorithm with regard to the radius was developed to minimize the SSOP. This paper provides a mathematical relationship which allows the radius to be optimized for a given UCA with a certain number of elements. The optimization algorithm is still valid for mutual coupling in practice, however, the optimum value needs to be calculated based on the NEC simulation data. In this work, it is assumed that Bob's location is known by Alice beforehand. In practice, there could be inaccuracy in Bob's location information at Alice, whether Bob sends his location to Alice or Alice estimates Bob's location. In future work, it can be extended to include the impact of error in Bob's location when optimizing the array parameters in practice. We will also extend our work considering random locations of Bob.

APPENDIX A CONVERSION OF OPTIMIZATION PROBLEM

Because $\theta_B \sim \mathcal{U}(0, 2\pi)$, $\text{err}(R)$ can be calculated by

$$\text{err}(R) = \frac{1}{2\pi} \int_0^{2\pi} (\bar{p} - \bar{p}_{\min}) d\theta_B. \quad (36)$$

To find the minimum value of $\text{err}(R)$, the zeros of the partial derivative of $\text{err}(R)$ with respect to R are calculated,

$$\frac{\partial}{\partial R} \text{err}(R) = 0 \quad (37)$$

$$\Rightarrow \frac{\partial}{\partial R} \frac{1}{2\pi} \int_0^{2\pi} (\bar{p} - \bar{p}_{\min}) d\theta_B = 0 \quad (38)$$

$$\Rightarrow \frac{1}{2\pi} \int_0^{2\pi} \left(\frac{\partial}{\partial R} \bar{p} - \frac{\partial}{\partial R} \bar{p}_{\min} \right) d\theta_B = 0. \quad (39)$$

Because \bar{p}_{\min} is a fixed value for certain θ_B and only depends on θ_B , the partial derivative $\frac{\partial}{\partial R} \bar{p}_{\min} = 0$. Thus, it can be derived that

$$\frac{\partial}{\partial R} \text{err}(R) = 0 \quad (40)$$

$$\Rightarrow \frac{1}{2\pi} \int_0^{2\pi} \frac{\partial}{\partial R} \bar{p} d\theta_B = 0 \quad (41)$$

$$\Rightarrow \frac{\partial}{\partial R} \frac{1}{2\pi} \int_0^{2\pi} \bar{p} d\theta_B = 0 \quad (42)$$

$$\Rightarrow \frac{\partial}{\partial R} \bar{p} = 0, \quad (43)$$

where \bar{p} is the averaged SSOP over Bob's angle and is defined by

$$\bar{p} = \frac{1}{2\pi} \int_0^{2\pi} \bar{p} d\theta_B. \quad (44)$$

Thus, we can obtain

$$R_{opt} = \arg \min_R \bar{p}. \quad (45)$$

APPENDIX B PROOF OF THEOREM 1

To obtain the upper bound \bar{p}_{up} , two instances of Jensen's inequality will be used to derive \bar{p}_{up} .

$$\mathbb{E}[e^X] \geq e^{\mathbb{E}[X]}, \quad (46)$$

where X is a random variable. The equality holds if and only if X is a deterministic value. The other one involved is expressed by

$$\mathbb{E}[X^{\frac{2}{\beta}}] \leq (\mathbb{E}[X])^{\frac{2}{\beta}}, \quad (47)$$

where X is a random variable and $\beta \geq 2$. The equality holds when $\beta = 2$ for any X .

The upper bound \bar{p}_{up} can be derived based on $\bar{p} \leq \bar{p}_{up}$. Using (12), it can be derived that

$$\begin{aligned} \bar{p} &= \mathbb{E}_{\theta_B}[\bar{p}] \leq \mathbb{E}_{\theta_B}[\bar{p}_{up}] \\ &= 1 - \mathbb{E}_{\theta_B} \left[\exp \left\{ -\lambda_e \pi \left[\frac{c_0 K}{2\pi(K+1)} A_0 + \frac{c_0}{K+1} \right]^{\frac{2}{\beta}} \right\} \right]. \end{aligned} \quad (48)$$

Using (46) and (47), it can be derived that

$$1 - \mathbb{E}_{\theta_B} \left[\exp \left\{ -\lambda_e \pi \left[\frac{c_0 K}{2\pi(K+1)} A_0 + \frac{c_0}{K+1} \right]^{\frac{2}{\beta}} \right\} \right] \quad (49)$$

$$< 1 - \exp \left\{ -\lambda_e \pi \mathbb{E}_{\theta_B} \left[\left[\frac{c_0 K}{2\pi(K+1)} A_0 + \frac{c_0}{K+1} \right]^{\frac{2}{\beta}} \right] \right\} \quad (50)$$

$$\leq 1 - \exp \left\{ -\lambda_e \pi \left[\frac{c_0 K}{2\pi(K+1)} \mathbb{E}_{\theta_B}[A_0] + \frac{c_0}{K+1} \right]^{\frac{2}{\beta}} \right\}. \quad (51)$$

The equality in (50) does not hold because θ_B is random in this case. Then, \bar{p}_{up} can be obtained by

$$\bar{p}_{up} = 1 - \exp \left\{ -\lambda_e \pi \left[\frac{c_0 K \bar{A}_0}{2\pi(K+1)} + \frac{c_0}{K+1} \right]^{\frac{2}{\beta}} \right\}, \quad (52)$$

where \bar{A}_0 is the expectation of A_0 over θ_B and is given by

$$\bar{A}_0 = \mathbb{E}_{\theta_B}[A_0] = \frac{1}{2\pi} \int_0^{2\pi} A_0 d\theta_B. \quad (53)$$

The above equation can be calculated from (26) by directly solving the integral. Because

$$\int_0^{2\pi} e^{j l N \theta_B} d\theta_B = 0, \text{ for } l \neq 0 \quad (54)$$

it can be obtained that

$$\bar{A}_0 = 2\pi \sum_{n=0}^{N-1} J_0^2(2kR \sin(\frac{n}{N}\pi)). \quad (55)$$

REFERENCES

- [1] A. Mukherjee, S. A. A. Fakoorian, J. Huang, and A. L. Swindlehurst, "Principles of physical layer security in multiuser wireless networks: A survey," *IEEE Commun. Surveys Tuts.*, vol. 16, no. 3, pp. 1550–1573, 3rd Quart., 2014.
- [2] Y. Liu, H.-H. Chen, and L. Wang, "Physical layer security for next generation wireless networks: Theories, technologies, and challenges," *IEEE Commun. Surveys Tuts.*, vol. 19, no. 1, pp. 347–376, 1st Quart., 2017.
- [3] A. D. Wyner, "The wire-tap channel," *Bell Syst. Tech. J.*, vol. 54, no. 8, pp. 1355–1387, 1975.

- 707 [4] J. Barros and M. R. Rodrigues, "Secrecy capacity of wireless channels,"
708 in *Proc. IEEE Int. Symp. Inf. Theory*, Jul. 2006, pp. 356–360.
- 709 [5] M. Bloch, J. Barros, M. R. D. Rodrigues, and S. W. McLaughlin, "Wire-
710 less information-theoretic security," *IEEE Trans. Inf. Theory*, vol. 54,
711 no. 6, pp. 2515–2534, Jun. 2008.
- 712 [6] S. Shafiee and S. Ulukus, "Achievable rates in Gaussian MISO channels
713 with secrecy constraints," in *Proc. IEEE ISIT*, Nice, France, Jun. 2007,
714 pp. 2466–2470.
- 715 [7] A. Khisti and G. W. Wornell, "Secure transmission with multiple
716 antennas I: The MISOME wiretap channel," *IEEE Trans. Inf. Theory*,
717 vol. 56, no. 7, pp. 3088–3104, Jul. 2010.
- 718 [8] A. Mukherjee and A. L. Swindlehurst, "Robust beamforming for security
719 in MIMO wiretap channels with imperfect CSI," *IEEE Trans. Signal
720 Process.*, vol. 59, no. 1, pp. 351–361, Jan. 2011.
- 721 [9] S. Yan and R. Malaney, "Location-based beamforming for enhancing
722 secrecy in rician wiretap channels," *IEEE Trans. Wireless Commun.*,
723 vol. 15, no. 4, pp. 2780–2791, Apr. 2016.
- 724 [10] S. Lakshmanan, C. L. Tsao, and R. Sivakumar, "Aegis: Physical space
725 security for wireless networks with smart antennas," *IEEE/ACM Trans.
726 Netw.*, vol. 18, no. 4, pp. 1105–1118, Aug. 2010.
- 727 [11] A. Sheth, S. Seshan, and D. Wetherall, "Geo-fencing: Confining Wi-Fi
728 coverage to physical boundaries," in *Proc. IEEE 7th Int. Conf. Pervasive
729 Comput.*, Nara, Japan, May 2009, pp. 274–290.
- 730 [12] N. Anand, S.-J. Lee, and E. W. Knightly, "STROBE: Actively securing
731 wireless communications using zero-forcing beamforming," in *Proc.
732 INFOCOM*, Mar. 2012, pp. 720–728.
- 733 [13] T. Wang and Y. Yang, "Enhancing wireless communication privacy with
734 artificial fading," in *Proc. IEEE 9th Int. Conf. Mobile Adhoc Sensor
735 Syst. (MASS)*, Oct. 2012, pp. 173–181.
- 736 [14] H. Li, X. Wang, and W. Hou, "Security enhancement in cooperative
737 jamming using compromised secrecy region minimization," in *Proc.
738 IEEE 13th Can. Workshop Inf. Theory*, Toronto, Canada, Jun. 2013,
739 pp. 214–218.
- 740 [15] J. Wang, J. Lee, F. Wang, and T. Q. Quek, "Jamming-aided secure com-
741 munication in massive MIMO Rician channels," *IEEE Trans. Wireless
742 Commun.*, vol. 14, no. 12, pp. 6854–6868, Dec. 2015.
- 743 [16] S. Sarma, S. Shukla, and J. Kuri, "Joint scheduling & jamming for data
744 secrecy in wireless networks," in *Proc. 11th Int. Symp. Modeling Optim.
745 Mobile, Ad Hoc Wireless Netw. (WiOpt)*, May 2013, pp. 248–255.
- 746 [17] W. Li, M. Ghogho, B. Chen, and C. Xiong, "Secure communi-
747 cation via sending artificial noise by the receiver: Outage secrecy
748 capacity/region analysis," *IEEE Commun. Lett.*, vol. 16, no. 10,
749 pp. 1628–1631, Oct. 2012.
- 750 [18] T.-X. Zheng, H.-M. Wang, and Q. Yin, "On transmission secrecy outage
751 of a multi-antenna system with randomly located eavesdroppers," *IEEE
752 Commun. Lett.*, vol. 18, no. 8, pp. 1299–1302, Aug. 2014.
- 753 [19] Y. Zhang, Y. Ko, R. Woods, and A. Marshall, "Defining spatial
754 secrecy outage probability for exposure region-based beamforming,"
755 *IEEE Trans. Wireless Commun.*, vol. 16, no. 2, pp. 900–912, Feb. 2017.
- 756 [20] B. Friedlander and A. J. Weiss, "Direction finding in the presence
757 of mutual coupling," *IEEE Trans. Antennas Propag.*, vol. 39, no. 3,
758 pp. 273–284, Mar. 1991.
- 759 [21] J. Dai, X. Bao, N. Hu, C. Chang, and W. Xu, "A recursive RARE
760 algorithm for DOA estimation with unknown mutual coupling," *IEEE
761 Antennas Wireless Propag. Lett.*, vol. 13, pp. 1593–1596, Aug. 2014.
- 762 [22] Y. Zhang, B. Yin, R. Woods, J. Cavallaro, A. Marshall, and Y. Ko,
763 "Investigation of secure wireless regions using configurable beamform-
764 ing on WARP," in *Proc. IEEE 48th Asilomar Conf. Signals, Syst.
765 Comput.*, Nov. 2014, pp. 1979–1983.
- 766 [23] B. Allen and M. Ghavami, *Adaptive Array Systems: Fundamentals and
767 Applications*. Hoboken, NJ, USA: Wiley, 2006.
- 768 [24] X. Zhou, M. R. McKay, B. Maham, and A. Hjørungnes, "Rethinking the
769 secrecy outage formulation: A secure transmission design perspective,"
770 *IEEE Commun. Lett.*, vol. 15, no. 3, pp. 302–304, Mar. 2011.
- 771 [25] Y. Zhang, Y. Ko, R. Woods, A. Marshall, J. Cavallaro, and K. Li, "On
772 spatial security outage probability derivation of exposure region based
773 beamforming with randomly located eavesdroppers," in *Proc. IEEE 50th
774 Asilomar Conf. Signals, Syst. Comput.*, Nov. 2016, pp. 689–690.
- 775 [26] G. J. Burke, A. J. Poggio, J. C. Logan, and J. W. Rockway, "Numerical
776 electromagnetic code (NEC)," in *Proc. IEEE Int. Symp. Electromagn.
777 Compat.*, Livermore, CA, USA, Oct. 1979, pp. 1–3.
- 778 [27] M. Ghogho and A. Swami, "Physical-layer secrecy of MIMO communi-
779 cations in the presence of a Poisson random field of eavesdroppers," in
780 *Proc. IEEE Int. Conf. Commun. (ICC)*, Kyoto, Japan, Jun. 2011, pp. 1–5.
- 781 [28] F. Gross, *Smart Antennas for Wireless Communications With MATLAB*.
782 New York, NY, USA: McGraw-Hill, 2005.
- [29] *FCI-3710 Phased Array Antenna*. Accessed: Oct. 25, 2017. 783
[Online]. Available: [http://www.fidelity-comtech.com/wp-content/](http://www.fidelity-comtech.com/wp-content/uploads/SpecSheet_FCI-3710.pdf) 784
[uploads/SpecSheet_FCI-3710.pdf](http://www.fidelity-comtech.com/wp-content/uploads/SpecSheet_FCI-3710.pdf) 785
- [30] K. R. Dandekar, H. Ling, and G. Xu, "Effect of mutual coupling on 786
direction finding in smart antenna applications," *Electron. Lett.*, vol. 36, 787
no. 22, pp. 1889–1891, Oct. 2000. 788
- [31] H. Singh, H. Sneha, and R. Jha, "Mutual coupling in phased 789
arrays: A review," *Int. J. Antennas Propag.*, vol. 2013, Mar. 2013, 790
Art. no. 348123. 791 AQ:4



Yuanrui Zhang received the B.Sc. degree in communication engineering from Shandong University, China, in 2009, the M.Sc. degree in communication and information technology from the University of Bremen, Germany, in 2012, and the Ph.D. degree in wireless innovation from Queen's University Belfast, U.K., in 2016. He is actively involved with areas in wireless communications, such as physical layer security, beamforming, and channel coding.



Roger Woods (M'95–SM'01) received the B.Sc. degree (Hons.) in electrical and electronic engineering and the Ph.D. degree from Queen's University Belfast in 1985 and 1990, respectively. He is currently a Full Professor with Queen's University Belfast, where he created and leads the Programmable Systems Laboratory. He has co-founded a spin-off company, Analytics Engines Ltd., which looks to exploit programmable systems research. His research interests are in heterogeneous programmable systems and system level design tools for data, signal and image processing, and telecommunications. He holds four patents and has authored over 200 papers. He is a member of the IEEE Signal Processing and Industrial Electronics Societies. He is on the Advisory Board for the IEEE SPS Technical Committee on the Design and Implementation of Signal Processing Systems. He is on the Editorial Board for the *ACM Transactions on Reconfigurable Technology and Systems*, the *Journal of VLSI Signal Processing Systems*, and the *IET Proceedings on Computer and Digital Techniques*. He was the General Chair for the 2014 Asilomar IEEE Conference on Signals, Systems, and Computers and is on the program committees of a number of IEEE conferences.



Youngwook Ko received the B.S.E. degree in information and communications engineering from Hannam University, South Korea, and the M.S. and Ph.D. degrees in electrical engineering from Arizona State University, Tempe, AZ, USA, in 2002 and 2006, respectively. He was with Samsung for two years, as a Senior Researcher. In 2008, he was with the Electrical and Computer Engineering Department, University of Alberta, Canada. From 2010 to 2013, he was with CCSR, University of Surrey, U.K., as a Senior Research Fellow. Since 2013, he has been with the ECIT Institute, Queen's University Belfast, as a Lecturer. He has authored over 40 publications in major IEEE international journals and peer-reviewed international conferences. He is a pioneer of index modulation techniques, and his current research include the areas of index modulation OFDM, sporadic machine type communications, physical wireless security, and the next generation wireless manufacturing systems. He was a recipient of several EPSRC and Newton projects, such as the EPSRC First Grant Award and the EPSRC IDS. He is a member of the EPSRC Peer-Review Associate College and is on the Editorial Board of the *Journal on Physical Communications* (Elsevier).

843
844
845
846
847
848
849
850
851
852
853
854
855
856
857
858
859
860
861
862
863
864



Alan Marshall (M'88–SM'00) has spent over 24 years of experience in the telecommunications and defense industries. He has been a Visiting Professor in network security with the University of Nice Sophia Antipolis/CNRS, France, and an Adjunct Professor of research with Sunway University Malaysia. He has authored over 200 scientific papers and holds a number of joint patents in the areas of communications and network security. His research interests include network architectures and protocols, mobile and wireless networks, network security, high-speed packet switching, quality of service and experience architectures, and distributed haptics. He is a fellow of the Institution of Engineering and Technology. He is currently the Chair in Communications Networks with the University of Liverpool, where he is also the Director of the Advanced Networks Group. He has formed a successful spin-out company, Traffic Observation & Management Ltd., specializing in intrusion detection and prevention for wireless networks. He is a Section Editor (section B: *Computer and Communications Networks and Systems*) for the *Computer Journal of the British Computer Society*, a member of the Editorial Board of the *Journal of Networks*, and on the program committees of a number of IEEE conferences.



Junqing Zhang received the B.Eng. and M.Eng. degrees in electrical engineering from Tianjin University, China, in 2009 and 2012, respectively, and the Ph.D. degree in electronics and electrical engineering from Queen's University Belfast, U.K., in 2016. He is currently a Post-Doctoral Research Fellow with Queen's University Belfast. His research interests include physical layer security and OFDM.

865
866
867
868
869
870
871
872

IEEE PROOF

AUTHOR QUERIES

AUTHOR PLEASE ANSWER ALL QUERIES

PLEASE NOTE: We cannot accept new source files as corrections for your paper. If possible, please annotate the PDF proof we have sent you with your corrections and upload it via the Author Gateway. Alternatively, you may send us your corrections in list format. You may also upload revised graphics via the Author Gateway.

AQ:1 = Please be advised that per instructions from the Communications Society this proof was formatted in Times Roman font and therefore some of the fonts will appear different from the fonts in your originally submitted manuscript. For instance, the math calligraphy font may appear different due to usage of the `usepackage[mathcal]euscript`. We are no longer permitted to use Computer Modern fonts.

AQ:2 = Please note that there were discrepancies between the accepted pdf [single.pdf] and the [5 manuscript.tex] in the sentences on line nos 48 and 49. We have followed [5 manuscript.tex].

AQ:3 = Note that if you require corrections/changes to tables or figures, you must supply the revised files, as these items are not edited for you.

AQ:4 = Please confirm the volume no. for ref. [31].

IEEE PROOF